July 10, 2024
Volume 146
Number 27
pubs.acs.org/JACS

JACS

JOURNAL OF THE AMERICAN CHEMICAL SOCIETY

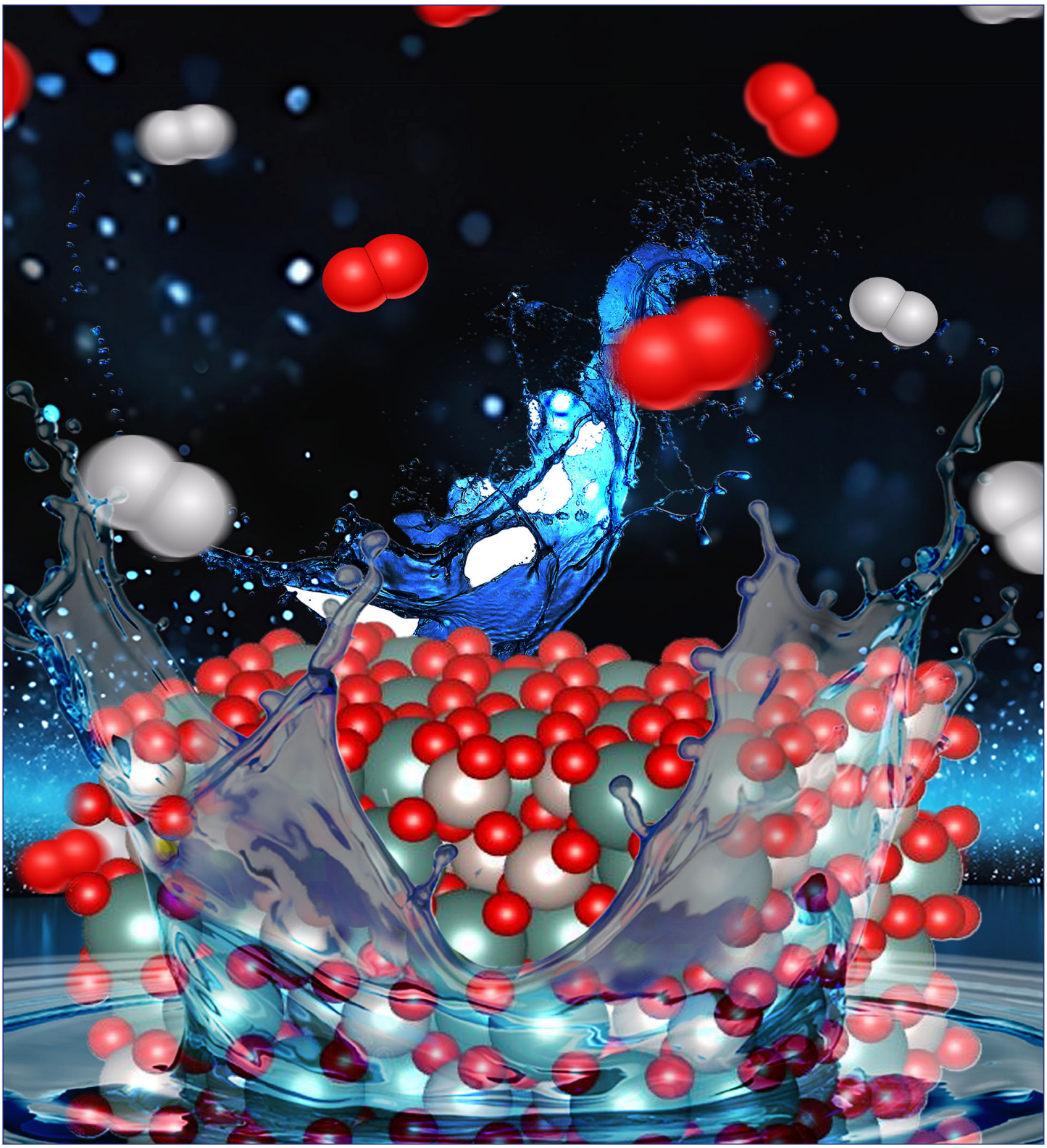

ACS Publications
Most Trusted. Most Cited. Most Read.

www.acs.org

JACS
JOURNAL OF THE AMERICAN CHEMICAL SOCIETY
pubs.acs.org/JACS
Article

Defect Engineering in Composition and Valence Band Center of $Y_2(Y_xRu_{1-x})_2O_{7-\delta}$ Pyrochlore Electrocatalysts for Oxygen Evolution Reaction

Bidipta Ghosh, Cheng Zhang, Stefanie Frick, En Ju Cho, Toby Woods, Yujie Yang, Nicola H. Perry, Andreas Klein, and Hong Yang*

Cite This: J. Am. Chem. Soc. 2024, 146, 18524−18534

Read Online

ACCESS | Metrics & More | Article Recommendations | Supporting Information

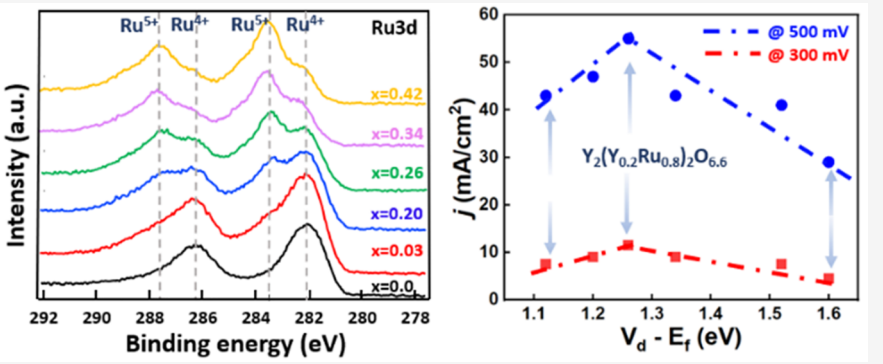

ABSTRACT: Oxygen evolution reaction (OER) takes place in various types of electrochemical devices that are pivotal for the conversion and storage of renewable energy. This paper describes a strategy in the design of solid-state structures of OER electrocatalysts through controlling the cation substitution on the active metal site and consequently valence band center position of site-mixed $Y_2(Y_xRu_{1-x})_2O_{7-\delta}$ pyrochlore to achieve high catalytic activity. We found that partially replacing the B-site Ru^{4+} cation with A-site Y^{3+} in pyrochlore-structured $Y_2Ru_2O_{7-\delta}$ modifies the oxidation state of B-site Ru from 4^+ to 5^+, as observed by electron paramagnetic resonance (EPR) spectroscopy but does not continuously increase the oxygen vacancy concentration in these oxygen substoichiometric compositions, as quantified by thermogravimetric analysis (TGA) decomposition studies. We found the increased Ru oxidation state leads to a downshift in valence band center. X-ray photoelectron spectroscopy (XPS) analysis was performed to quantitatively determine the optimal band center to be ∼1.27 eV below the Fermi energy level based on the analysis of the valence band edge of these Ru-based $Y_2(Y_xRu_{1-x})_2O_{7-\delta}$ OER electrocatalysts. This work highlights that defect engineering can be a practical, effective approach to the optimization of oxidation state and electronic band center for high OER catalytic performance in a quantitative manner.

INTRODUCTION

Hydrogen is an energy carrier that has the potential to play a crucial role in the carbon neutral society.[1−12] A proton exchange membrane (PEM)-based water electrolyzer may produce high-purity hydrogen gas at high current density with low ohmic loss because of the high ionic conductivity.[13−17] It also has a compact design, a fast system response, and low energy consumption. These attributes make the PEM-based water electrolyzer one of the most attractive devices to produce green hydrogen.[1,2,18,19] Under acidic operating conditions, water molecules are oxidized at the anode to generate oxygen (O_2), which is called the oxygen evolution reaction (OER).[1,20,21] A large overpotential is often required for OER due to the slow electron transfer in various elemental steps, which result in sluggish kinetics.[21−30] Therefore, efficient electrocatalysts are needed to lower the reaction kinetic barrier and accelerate the water splitting by reducing the OER overpotential.[1,12,31,32]

Oxide, hydroxide, carbide, and nitride electrocatalysts have been tested for their electrocatalytic properties, though many suffer from degradation under acidic and oxidative reaction conditions. The commercially available OER electrocatalysts are largely composed of Ir elements (i.e., Ir and IrO_2), because of their good activity and durability.[33−35] The scarcity of Ir however makes it hard for widespread industrial applications at

Received: March 27, 2024
Revised: May 1, 2024
Accepted: May 21, 2024
Published: May 31, 2024

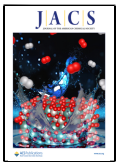

https://doi.org/10.1021/jacs.4c04292
J. Am. Chem. Soc. 2024, 146, 18524−18534

large scale. Thus, there is a need to develop non-Ir-based OER electrocatalysts for hydrogen generation through water splitting.[36] Ruthenium-based electrocatalysts exhibit numerous benefits, such as high activity, universality across pH levels, and the most economical cost within the noble metal category.[37,38]

The design of electrocatalysts has been focused on changing the composition and geometric and electronic structures to promote the various electron transfer processes.[39,40] Recently, complex oxides ($A_xB_yO_z$) have been examined for their use as OER electrocatalysts under acidic conditions.[41−43] Among various complex oxides, pyrochlores have gained attention as exceptionally effective and durable substances that serve as both catalysts and conductive foundations for hybrid catalyst systems. The adaptable composition of pyrochlore oxides offers numerous avenues for enhancing electrocatalytic performance through the control and alteration of material structures and characteristics.[44,45] We showed that pyrochlore $Y_2Ru_2O_7$ could have both high activity and stability.[41] The ability to modify the active site (Ru) is thought to be a key feature for enhanced OER activity, while an A-site yttrium cation helps stabilize the chemical bond between Ru and lattice O. In situ X-ray absorption spectroscopy (XAS) studies indicate the B-site Ru metal cation likely exists in a multivalent fashion.[46−48] Among pyrochlore-type $A_2B_2O_7$ electrocatalysts, nonstoichiometric, complex oxides such as $Y_2(Ru_xMn_{1-x})_2O_7$ and $Y_2(Ir_xMn_{1-x})_2O_7$ could exhibit high OER activity.[49] High activity has often been correlated to a high degree of atomic disordering. Such results strongly indicate defect-engineered nanomaterials may have great potential for achieving excellent reactivity and selectivity for electrocatalysis.[50,51]

While quantum simulations such as density functional theory (DFT) calculations have made a great attempt to understand the structure−property relationships, complexity in metal oxides often makes it prohibitively difficult to predict the right global electron band structures for OER performance. In addition, point defects and the nonstochiometric nature of the surface create additional hurdles for designing the composition based on quantum simulation techniques. Thus, development of the right defect engineering approach and the characterization method could be critical to the realization of the design of high-performing OER catalysts.[52]

For defect engineering of metal oxides, one popular method is aliovalent doping, replacing a high-valence cation with a lower valence element.[53−56] Introduction of a lower oxidation state cation ($A^{(n-1)+}$) onto a higher oxidation state cation (B^{n+}) site generates acceptors (A'_B), which could be charge-compensated through formation of positive defects, such as ionized oxygen vacancies ($v_O^{\cdot\cdot}$) [55] or trapped holes leading to a higher valence state (e.g., $B^{(n+1)+}$). These responses can be described in the Y−Ru−O pyrochlore system by the following equations using the Kröger−Vink notation:

Oxygen vacancy creation:

$$2Y_2O_3 \xrightarrow{Y_2Ru_2O_7} 2Y_Y^{\times} + 2Y'_{Ru} + 6O_O^{\times} + v_O^{\bullet\bullet} \quad (1)$$

Generation of holes:

$$2Y_2O_3 + \frac{1}{2}O_2(g) \xrightarrow{Y_2Ru_2O_7} 2Y_Y^{\times} + 2Y'_{Ru} + 7O_O^{\times} + 2h^{\bullet} \quad (2)$$

Trapping of holes on Ru:

$$Ru_{Ru}^{\times} + h^{\bullet} \rightarrow Ru_{Ru}^{\bullet} \quad (3)$$

Change of defect concentrations through substitution may also affect the band center position of the active metal site. The up- and down-shifting in the band center may accelerate the adsorption and desorption of active intermediates, thus the catalytic activity.[57−60]

In this study, we demonstrate that atomic mixing at the active site in a complex oxide (i.e., B-site of pyrochlore) can be an effective method in defect engineering to achieve the global solid-state structure that has high OER activity. Specifically, we successfully partially replaced Ru^{4+} at the B-site with A-site cation Y^{3+} in the $Y_2(Y_xRu_{1-x})_2O_{7-\delta}$ series. We quantified the as-prepared, overall room-temperature oxygen substoichiometry, δ, as a function of increasing Y content, x, through decomposition thermogravimetric analysis across the series. Besides the more commonly observed cubic phase of pyrochlore $Y_2Ru_2O_{7-\delta}$, we also succeeded in making and confirming a less known orthorhombic phase $Y_3RuO_{7-\delta}$. In addition to the observed evidence of oxygen deficiency, the mixed B-site compounds were shown to result in the partial change of the Ru average cation valence state and a shift in the d-band center that was experimentally quantified. XPS studies suggest the electron distribution is due to the mixed valence ($4^+/5^+$) of Ru cations, and the optimal Ru valence band center was found to be 1.27 eV below the Fermi energy to reach the highest OER performance.

EXPERIMENTAL SECTION

Material Synthesis. A pyrochlore-type $Y_2(Y_xRu_{1-x})_2O_{7-\delta}$ electrocatalyst was synthesized via the sol−gel method. To be specific, predetermined, stoichiometric amounts of $Y(NO_3)_3{\cdot}6H_2O$ and $Ru(NO)(NO_3)_x(OH)_y$ (Table S1) were mixed with 10 mL of deionized (DI) water in a 50 mL beaker while stirring, followed by addition of citric acid (4 mmol, 0.8406 g). The beaker was then transferred to an aluminum heating block at 80 °C and kept at this temperature overnight to evaporate the water. The beaker was then placed in a vacuum oven (VWR Symphony, ∼10 mmHg) at 80 °C for an additional 3−4 h to remove the residual amount of water. The obtained solid was then ground into powder using a mortar and pestle, heated up to 600 °C at a rate of 5 °C/min in a tube furnace (TF55035A-1, Lindberg/Blue M), and maintained at this temperature for 6 h. After being cooled down to room temperature, the calcinated sample was ground to a fine powder, which was placed in a ceramic boat and transferred to another tube furnace, heated to 1000 °C at a rate of 5 °C/min, and maintained at this temperature for 12 h.

Material Characterization. Powder X-ray diffraction (PXRD) patterns were measured using either a Rigaku Miniflex 600 diffractometer with a Cu Kα X-ray source (λ = 1.54056 Å) at a scan rate of 0.01° 2θ per second or a Bruker D8 Advance system with a panoramic Soller slit and Cu Kα radiation at a step size of 0.01° 2θ and a hold time per step of 0.1 s.

Scanning electron microscopy (SEM) images were obtained using a Hitachi S4700 microscope at an acceleration voltage of 15 kV. The SEM specimen was prepared by depositing the catalyst powder on carbon tape on an SEM stub. Transmission electron microscopy (TEM) micrographs were obtained using a JEOL 2100 Cryo TEM with a LaB_6 emitter at 200 kV. The powdered sample was added to ethanol in a vial and sonicated for 30 min for dispersion. Then 10 μL of the sample was dropped onto a copper grid, which was used to obtain the TEM image. Energy dispersive X-ray fluorescence (XRF) was performed on a Shimadzu EDX-700 spectrometer with a Rh X-ray source. X-ray photoelectron spectroscopy (XPS) analysis was performed using a Physical Electronics PHI 5700 spectrometer with a monochromated Al Kα X-ray source to determine the binding energy. Binding energies are given with respect to the Fermi energy, which was calibrated using a metallic Ag standard. All samples were directly measured on the FTO substrate. Samples have been heated in 0.5 Pa O_2 at 400 °C for 1 h to remove carbonaceous species to avoid

https://doi.org/10.1021/jacs.4c04292
J. Am. Chem. Soc. 2024, 146, 18524−18534

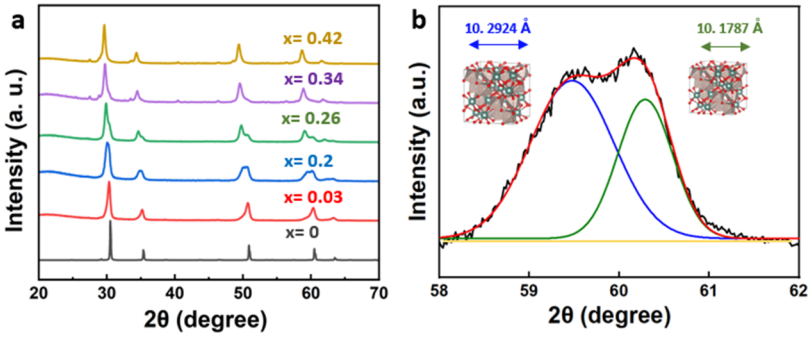

Figure 1. (a) PXRD patterns of $Y_2(Y_xRu_{1-x})_2O_{7-\delta}$ electrocatalysts (x = 0, 0.03, 0.2, 0.26, 0.34, and 0.42) and (b) the peak fitting of $Y_2(Y_{0.2}Ru_{0.8})_2O_{7-\delta}$ between 58° and 62° 2θ.

superposition the C 1s with Ru 3d emission (this is important as otherwise the Ru 3d peak would be superimposed with the C 1s emission). Smoothened spectra of valence bands were performed for better visualization of the changes using Origin Pro software. Specifically, we used Lowess (locally weighted scatterplot smoothing) in this study. The valence band center however was calculated using the unsmoothened raw spectra, so the smoothening does not affect the actual result. Electron paramagnetic resonance (EPR) data were obtained at a temperature of 10 K under He, using a Bruker 10″ EMXPlus X-band continuous wave EPR. Data under both parallel and perpendicular modes were recorded.

Preparation of Ink and Working Electrode for Electrochemical Measurement. Four milligrams of catalyst powder and 4 mg of Vulcan carbon XC-72 were ground together. The resulting powder was added to 1 mL of tetrahydrofuran (THF, HPLC grade, J.T. Baker) and 20 μL of 117 aqueous Nafion solution (5%, Sigma-Aldrich) and then sonicated for 30 min in an ice bath to obtain a homogeneous mixture. One mL of THF and 20 mL of Nafion were mixed to obtain a blank solution. Then, 6 μL of the catalyst ink was drop-cast onto a rotating disk electrode (RDE) and dried slowly to form a uniform thin film on the working electrode. After the ink dried, 10 μL of blank solution was drop-cast on the working electrode and dried in air to form a uniform thin film electrode.

Measurement of Electrochemical Performance. A homemade three-electrode cell was used to measure the electrochemical performance using a CHI 760B potentiostat (CH Instruments, Inc.). The cell is comprised of a hydrogen reference electrode (HydroFlex, Gaskatel), a platinum foil counter electrode (area: 1 × 1 cm^2), and a glassy carbon working electrode (surface area: 0.196 cm^2). The electrolyte used is a 0.1 M $HClO_4$ aqueous solution. The electrolyte was purged with hydrogen gas until saturation, and then the RHE was calibrated in H_2-saturated electrolyte solution before testing. After the calibration was done, the electrolyte was purged with O_2 for 30 min, and all measurements were performed under that condition. Cyclic voltammetry (CV) was measured at a scan rate of 10 mV/s between 1.1 and 1.8 V. The RDE rotating speed was set at 1600 rpm.

AC Impedance Measurement. Electrochemical impedance spectroscopy (EIS) measurements were performed at a potential higher than the onset potential of each of the catalysts (1.58 V), with a frequency range from 1 × 10^4 to 0.1 Hz. For each test, 10 μL of ink was deposited onto the RDE. The impedance spectra were presented in the form of Nyquist plots, having the real component of the impedance on the x-axis (Z′) and negative of the imaginary component on the y-axis (−Z″). The obtained data were fit using ZView software. The equivalent circuit of EIS data consists of three components: solution resistance (R_{sol}), charge transfer resistance (R_{ct}), and double-layer capacitance (C_{dl}).[41] Constant phase element (CPE) was used instead of double-layer capacitance (C_{dl}) to account for nonideality in the system.

Thermogravimetric Analysis of Oxygen Stoichiometry. The average oxygen substoichiometries (δ) of pyrochlore $Y_2(Y_xRu_{1-x})_2O_{7-\delta}$ powders were determined using a home-built thermogravimetric analysis (TGA) setup equipped with an XPR6UD5 microbalance (Mettler-Toledo) and vertical tube furnace (Mellen). The sample temperature was measured by an S-type thermocouple, and the oxygen partial pressures were determined by a lab-built Nernst-type zirconia oxygen sensor, placed close to the sample for accurate measurement. The analysis was performed under a flowing gas mixture of Ar/O_2 or $Ar/H_2/H_2O$ regulated by mass flow controllers (Alicat Scientific, Inc., USA), for precise control of pO_2. Both the buoyancy effect from temperature changes and the water uptake while changing the gas from dry to humid could potentially affect the accurate measurement of the solid mass. Therefore, their values were measured separately and subtracted from the sample measurement to calculate the mass changes deriving solely from changes in oxygen stoichiometry. The buoyancy effect from the temperature was corrected by using a reference alumina sample whose mass does not change with temperature. Averaged oxygen stoichiometries of the as-prepared powders at room temperature were analyzed because this is the most relevant condition for understanding the electrochemical performance. In a typical procedure, powder samples were held at 500 °C for drying and then cooled to 30−33 °C in a flow of Ar gas to obtain the initial masses in dry form. The powders were then reheated to 700 °C in a flow of Ar (where they remain pyrochlore) before switching isothermally to a gas mixture of 0.15% H_2 balanced with Ar, which was bubbled through water at 10 °C. The temperature of water in the bubbler was controlled by a circulating bath (ARCTIC A25B refrigerated circulators, ThermoFisher Scientific, USA) to set the humidity and thereby control the pO_2. Under these conditions, the pyrochlore phase was not stable, and it underwent decomposition to Ru and Y_2O_3, resulting in a large mass change as considerable oxygen was lost. Each condition was held until the sample mass reached a steady state. After the decomposition, the sample was reoxidized to Y_2O_3 and ∼RuO_2 by switching the gas mixture back to Ar and subsequently cooling.

RESULTS AND DISCUSSION

Structure of Mixed Pyrochlore-Type $Y_2(Y_xRu_{1-x})_2O_{7-\delta}$. Pyrochlore-structured $Y_2(Y_xRu_{1-x})_2O_{7-\delta}$ was synthesized via the sol−gel method. This method is advantageous over direct solid-state synthesis, as it produces sub-micron-sized particles. Compositions of these electrocatalysts were determined by XRF (Table S2). In a typical pyrochlore structure, Y^{3+} is at the center of an eight-coordinated dodecahedron, whereas Ru^{4+} is in a six-coordinated octahedron. Under the synthesis conditions used in this study, Y was successfully incorporated into the Ru site to create defects. Figure 1a shows PXRD patterns of the series of $Y_2(Y_xRu_{1-x})_2O_{7-\delta}$ electrocatalysts. All diffraction peaks of $Y_2Ru_2O_7$ (x = 0) can be assigned to the cubic phase pyrochlore in the $Fd3m$ space group. As Y cations incorporated into the B-site, the diffraction peak began to broaden and even split.

https://doi.org/10.1021/jacs.4c04292
J. Am. Chem. Soc. 2024, 146, 18524−18534

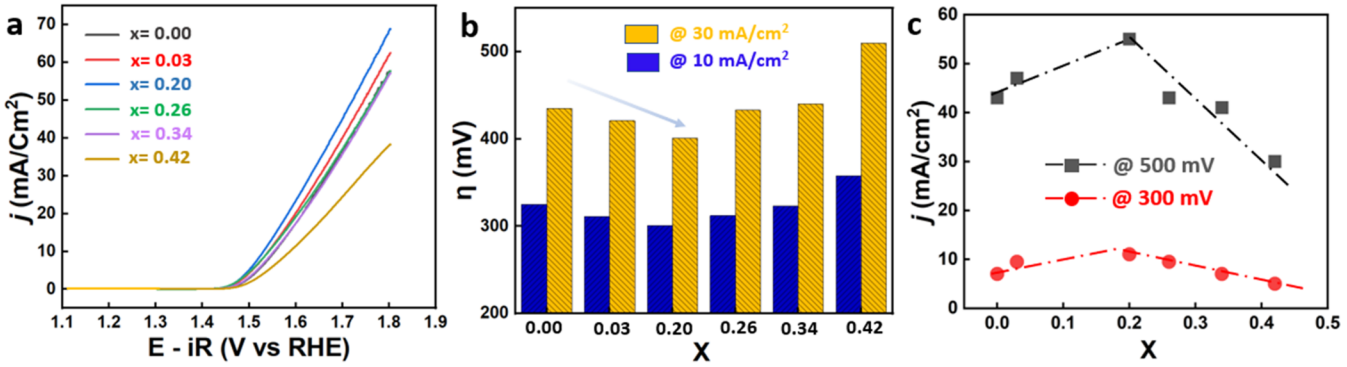

Figure 2. (a) CVs of $Y_2(Y_xRu_{1-x})_2O_{7-\delta}$ electrocatalysts and plots of their (b) overpotential and (c) current density as a function of mole fraction (x) of Y at the B-site.

For the $Y_2(Y_{0.03}Ru_{0.97})_2O_{7-\delta}$ sample, shoulder peaks were observed, suggesting the pyrochlores have two different dominant sizes of unit cells. When the x value increased to 0.2 in $Y_2(Y_{0.2}Ru_{0.8})_2O_{7-\delta}$, two sets of peaks became observable (Figure 1b). The split in the XRD pattern is attributed to the distortions in the cubic cell of pyrochlore. The low-angle peaks represent the defected, B-site mixed pyrochlores, suggesting dramatic changes occurring in structures. This result indicates that the B-site mixed electrocatalysts exist in pyrochlore structures, which were further analyzed by Rietveld refinement of the powder diffraction pattern (Figure S1). The unit cell lengths were calculated to be 10.246 Å for the defect-dominated forms and 10.148 Å for the less defected form of $Y_2(Y_{0.03}Ru_{0.97})_2O_{7-\delta}$. Similarly, the unit cell length of 10.292 Å is for the defected and 10.178 Å is for the less defected form of $Y_2(Y_{0.2}Ru_{0.8})_2O_{7-\delta}$. As the ionic radius of Y^{3+} (1.011 Å) is larger than that of Ru^{4+} (0.62 Å), the smaller cell parameter indicates low-level incorporation of Y^{3+} on the B (Ru) site, whereas a larger cell parameter indicates an appreciable amount of Y^{3+} on the B (Ru) site. We observed that when the x value increased to about 0.26, the mixed pyrochlore phases still dominated and were fit to two different cubic pyrochlore structures using the Rietveld refinement. The XRD patterns could be fit using the Rietveld refinement to two different cubic structures, which we attributed to distorted pyrochlores with a range of defect levels that appeared at two broad diffraction angles. A new orthorhombic phase was detected by PXRD when the x value increased to 0.34 ($Y_2(Y_{0.34}Ru_{0.66})_2O_{7-\delta}$) or higher. The SEM image shows these electrocatalysts were made of granular and sub-micrometer-sized uniform particles (Figure S2). TEM micrographs exhibit an increase in d-spacing from 2.76 Å for x equal to zero (cubic $Y_2Ru_2O_7$) to 2.95 Å for x equal to 0.42 in this series of $Y_2(Y_xRu_{1-x})_2O_{7-\delta}$ electrocatalysts (Figure S3). This observed change in d-spacing with increasing Y content agrees well with the XRD results, in which the relevant diffraction peaks shifted toward lower angles. A TEM study also indicates all solid electrocatalysts are highly crystalline.

OER Electrocatalytic Performance in Acid. Performances of these electrocatalysts were studied by using the three-electrode system with RDE as the working electrode. Figure 2a shows the polarization curves of $Y_2(Y_xRu_{1-x})_2O_{7-\delta}$ in a 0.1 M $HClO_4$ aqueous electrolyte. The results show initially that the OER activity increases with the increasing amount of Y at the B-site, reaching the highest current density (j) at the Y/Ru atomic ratio of 1/4 (or 0.2/0.8) on the B-site. This observation suggests the incorporation of a large Y^{3+} cation into the B-site changed the crystal structure in a way that accelerates the OER kinetics. When the Y/Ru atomic ratio further increased to 0.3/0.7, the OER activity started to decrease. Figure 2b shows the change in overpotential as a function of atomic fraction of Y at the B-site (x) at a current density of 10 and 30 mA/cm^2, respectively. Tafel analysis shows that the $Y_2(Y_{02}Ru_{0.8})_2O_{7-\delta}$ electrocatalyst has a smallest Tafel slope (Figure S4). The trend in Tafel slope is in good agreement with that in OER overpotential for these B-site-mixed pyrochlore electrocatalysts. As the morphology and particle sizes of these $Y_2(Y_xRu_{1-x})_2O_{7-\delta}$ pyrochlores are similar, this observation suggests that the change of the reaction kinetics could stem from their electronic structure. Figure 2c illustrates the relationship between mole fraction of Y at the B-site and current density at two different overpotentials, showing a volcano shape with maximum performance at x equal to 0.2. The chronopotentiometry plot exhibits that the $Y_2(Y_{02}Ru_{0.8})_2O_{7-\delta}$ electrocatalyst is stable for at least 60 h, determined at a current density of 10 mA/cm^2 (Figure S5).

We measured the CV curves in the nonfaradaic potential region between 1.13 and 1.23 V vs RHE at scan rates of 10, 20, 30, 40, 50, and 60 mV s^{-1}, respectively, to determine the double-layer capacitance C_{dl} values (Figure S6). The C_{dl} values were obtained from the slope in the plot of current density differences ($\Delta j/2$) as a function of scan rate at 1.18 V vs RHE (Figure S7). The results show these electrocatalysts have close C_{dl} values between 2 and 3 mF cm^{-2}, although the $Y_2(Y_{0.03}Ru_{0.97})_2O_{7-\delta}$ electrocatalyst exhibits the largest C_{dl} of 2.93 mF cm^{-2}, followed by $Y_2(Y_{0.2}Ru_{0.8})_2O_{7-\delta}$ (2.73 mF cm^{-2}) and $Y_2Ru_2O_7$ (2.31 mF cm^{-2}).This analysis further indicates that electrochemical surface area (ECSA) does not significantly contribute to the volcano-shaped performance trend of these defect-engineered pyrochlore ruthenates. Electrochemical impedance spectroscopy measurement was performed to understand the OER catalytic property. Figure 3 shows the Nyquist plots of $Y_2(Y_xRu_{1-x})_2O_{7-\delta}$ electrocatalysts measured at 1.58 V in 0.1 M $HClO_4$. The corresponding equivalent electrical circuit comprises solution resistance (R_{sol}), charge transfer resistance (R_{ct}), and double-layer capacitance (C_{dl}), and the results are summarized in Table S3. The R_{ct} value shows a strong correlation with the OER performance, with $Y_2(Y_{0.2}Ru_{0.8})_2O_{7-\delta}$ exhibiting the lowest R_{ct} value of 8.278 Ω, followed by $Y_2(Y_{0.03}Ru_{0.97})_2O_{7-\delta}$ (9.265 Ω) and the parent compound $Y_2Ru_2O_{7-\delta}$ (13.79 Ω). It appears that $Y_2(Y_{0.2}Ru_{0.8})_2O_{7-\delta}$ has the lowest resistance to charge transfer, which might contribute to the enhanced catalytic activity.[61]

https://doi.org/10.1021/jacs.4c04292
J. Am. Chem. Soc. 2024, 146, 18524−18534

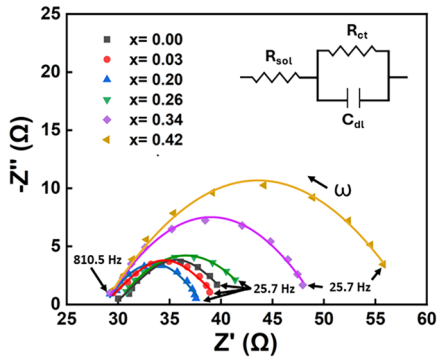

Figure 3. Nyquist plots of $Y_2(Y_xRu_{1-x})_2O_{7-\delta}$ electrocatalysts at 1.58 V in 0.1 M $HClO_4$. Increasing frequency (ω) direction is indicated. The solid line represents equivalent circuit fit.

Study of Structure−Property Relationship Using XPS, EPR, and TGA. XPS survey spectra was recorded in the binding energy (BE) range between 1 and 1400 eV to analyze the surface composition of these electrocatalysts (Figure S8). Figure 4 shows XPS spectra in the Ru 3d region for both the

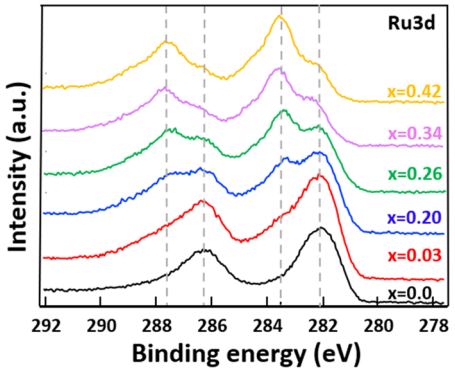

Figure 4. XPS spectra in the Ru 3d region of the $Y_2(Y_xRu_{1-x})_2O_{7-\delta}$ electrocatalysts.

parent compound and B-site-engineered $Y_2(Y_xRu_{1-x})_2O_{7-\delta}$ electrocatalysts. The peak centered at 282 eV is about 1 eV higher than that of Ru^{4+} in RuO_2. This difference comes from the metallic behavior of RuO_2 and the semiconducting one of $Y_2(Y_xRu_{1-x})_2O_{7-\delta}$. With increasing Y substitution, an additional peak at 283.7 eV evolved, which can be assigned to a higher oxidation state. The observation of two XPS peaks at 282 and 283.7 eV, respectively, indicates the presence of two Ru oxidation states in the defect-engineered pyrochlore electrocatalysts. In Figure S9, Y 3d peaks are centered at 158.5 and 156.5 eV that resemble those of Y $3d_{3/2}$ and $3d_{5/2}$. The Y 3d peaks exhibit only some broadening with increasing Y content, but no clear asymmetry is observed. Y remains 3^+ independent of the amount on the B-site. The difference in binding energy of the regular Y on the A-site and that on the Ru site (B-site) is evidently too small to be resolved. The O 1s spectra show no major changes with increasing Y content (Figure S10). A concurrent broadening is also observed in the O 1s spectra, indicating that it is not related to changes of chemical valences.

Electron paramagnetic resonance spectroscopy was performed to determine the oxidation state of Ru species in parent compound $Y_2Ru_2O_{7-\delta}$ and defect-engineered pyrochlore $Y_2(Y_{0.2}Ru_{0.8})_2O_{7-\delta}$, electrocatalysts (Figure 5). The EPR spectra show that $Y_2Ru_2O_{7-\delta}$ does not exhibit prominent features in the perpendicular mode, whereas $Y_2(Y_{0.2}Ru_{0.8})_2O_{7-\delta}$ has a zero-crossing feature (Figure 5a). Well-defined peaks could be detected for both the parent and B-site mixed pyrochlores in a parallel mode (Figure 5b). This result indicates that while it mainly has one valence state in $Y_2Ru_2O_{7-\delta}$, the Ru cation has mixed valence states in the defect-engineered $Y_2(Y_{0.2}Ru_{0.8})_2O_{7-\delta}$ electrocatalyst. Assuming an octahedral ligand field for the Ru cation in $Y_2Ru_2O_7$, the zero-crossing feature should be observed for the species with integer spin number S in parallel mode of the EPR spectrum (Ru^{4+}, $S = 1$) (Figures 5c), while a half-integer spin species is active in the perpendicular mode measurement of EPR (Ru^{5+}, $S = 3/2$) (Figure 5d). Thus, the EPR data in parallel mode indicate that $Y_2Ru_2O_{7-\delta}$ largely has an integer spin system, which is Ru^{4+} ($S = 1$ for low-spin state and $S = 2$ for high-spin state). For the perpendicular mode, the EPR measurement is expected to show signals for the $S = 1/2$ or $3/2$ spin system which observed in $Y_2(Y_{0.2}Ru_{0.8})_2O_{7-\delta}$. A large g value and broad EPR signal indicate a spin−orbit coupling of Ru, and the unpaired electron is Ru centered.[62] Collectively, the EPR data confirm the presence of the Ru^{5+} oxidation state only in $Y_2(Y_{0.2}Ru_{0.8})_2O_{7-\delta}$. The existence of a similar zero crossing feature for the electrocatalysts indicates that both $Y_2Ru_2O_{7-\delta}$ and $Y_2(Y_{0.2}Ru_{0.8})_2O_{7-\delta}$ have a Ru^{4+} oxidation state. Thus, the observed enhancement in OER activity can be attributed in part to the mixed valence of Ru ($4^+/5^+$).[46,48,63−65]

We further examined the valence band position for Ru in this series of defect-engineered pyrochlore electrocatalysts based on XPS analysis. As the mole fraction of Y substitution at B-site increases, the valence band center moves toward high BE values (Figure 6a). The raw valence band spectra are presented in Figure S11. The valence band center, V_d, of an electrocatalyst is calculated using the following formula:[66]

$$V_d = \frac{\int f(E)E\ dE}{\int f(E)\ dE} \tag{4}$$

Substituting the Ru cation with Y^{3+} shifts the band center to higher binding energy. The relationship between the valence band center position with respect to the Fermi level and the OER activity exhibits a volcano-shaped plot (Figure 6b). The downshifting of this band center of Ru reduces the adsorption energy of intermediates. This change in electronic structure results in the decrease in the band center for the Ru d-electron and O p-electron overlap, which results in the increase of Ru−O covalency. Increased Ru−O covalency accelerates electron transfer between the Ru cation and O adsorbates and helps extraction of an electron from oxygen, resulting in improved oxygen evolution kinetics.[67,68]

Further downshift in the band center from $Y_2(Y_{0.26}Ru_{0.74})_2O_{7-\delta}$ resulted in lowered OER kinetics. This decrease can be explained based on an electron interaction model where bonding and antibonding states are generated between the Ru d-band and O p-band.[69−71] The downshifted d-band center makes more antibonding states below the Fermi level, which results in Pauli repulsion and thereby weakened bond strength.[71] Therefore, the electrocatalysts can effectively adsorb neither water molecules nor the intermediates, resulting in the loss of the OER activity. This finding strongly suggests that modulation of the valence band through defect engineering should be done in such a way that the d-band center distance needs to be optimal from the Fermi level for defect-

https://doi.org/10.1021/jacs.4c04292
J. Am. Chem. Soc. 2024, 146, 18524−18534

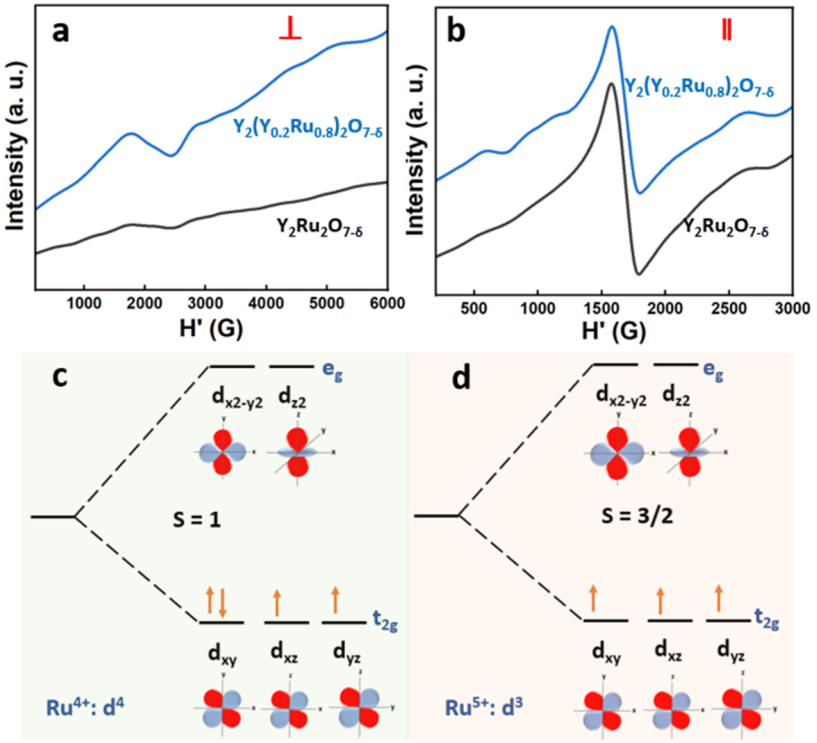

Figure 5. EPR spectra of $Y_2Ru_2O_{7-\delta}$ and $Y_2(Y_{0.2}Ru_{0.8})_2O_{7-\delta}$ pyrochloric electrocatalysts measured in (a) perpendicular and (b) parallel modes. Schematic of degenerated d-electronic configurations of (c) Ru^{4+} and (d) Ru^{5+} in an octahedral ligand field.

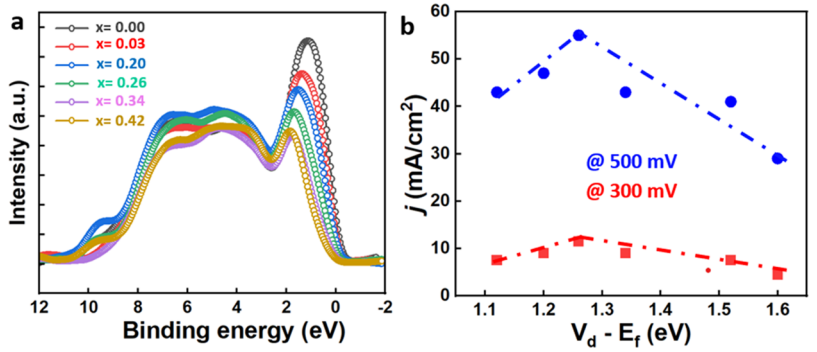

Figure 6. (a) Analysis of the Ru valence band and (b) the OER activity-band center relationship for electrocatalysts of defect-engineered pyrochlore $Y_2(Y_xRu_{1-x})_2O_{7-\delta}$.

engineered complex oxides to exhibit the highest catalytic activity.

Besides the cations, we carefully examined the oxygen defect chemistry in these pyrochlore electrocatalysts. Figure 7 displays the TGA data collected on three samples with varying Y/Ru ratios in $Y_2(Y_xRu_{1-x})_2O_{7-\delta}$, where x is equal to 0.03, 0.20, and 0.26, respectively. The black, red, and blue curves represent the mass change in response to temperature and oxygen partial pressure changes, sample temperature, and the log of oxygen partial pressure, respectively (Figure 7a–c). Expected pO_2 values below 700 °C are shown as dotted lines, since the Nernst-type O_2 sensor does not function well at low temperatures. When the pyrochlore powders were heated to 700 °C in dry Ar and switched to a H_2/Ar mixture, minor spikes in pO_2 were observed due to the residual O_2 gas in the gas line accompanying switching the gas from dry Ar to wet Ar and from wet Ar to a wet H_2/Ar mixture; these temporary sharp changes in pO_2 do not affect the results.

Note, in this experimental design pyrochlore samples were decomposed to Y_2O_3 and Ru at 700 °C and in the presence of a humid 0.15% H_2 and 99.85% Ar mixture. Yttrium oxide (Y_2O_3) is stable at 700 °C above a pO_2 of $\sim 10^{-50}$ atm,[72] and the Ru-RuO_2 pO_2 boundary is 9.9×10^{-8} atm at 700 °C, with Ru metal forming below this pO_2.[73] At this temperature and H_2/H_2O ratio of 0.124, the pO_2 value was determined experimentally using the Nernst-type sensor to be $(2.1-5.8) \times 10^{-19}$ atm, which agrees well with the theoretical value of 1×10^{-19} atm. After the decomposition step, the sample was reoxidized to Y_2O_3 and RuO_2 by switching the gas mixture back to Ar (**CAUTION**: *A controlled reoxidation was done to avoid possible ignition*). Figure S12 shows the XRD patterns after the decomposition and subsequent reoxidation steps in the TGA test. These data confirm the formation of Y_2O_3 and RuO_2 phases after reoxidation (vs Y_2O_3 and Ru under the decomposition conditions at lower oxygen partial pressure).

https://doi.org/10.1021/jacs.4c04292
J. Am. Chem. Soc. 2024, 146, 18524−18534

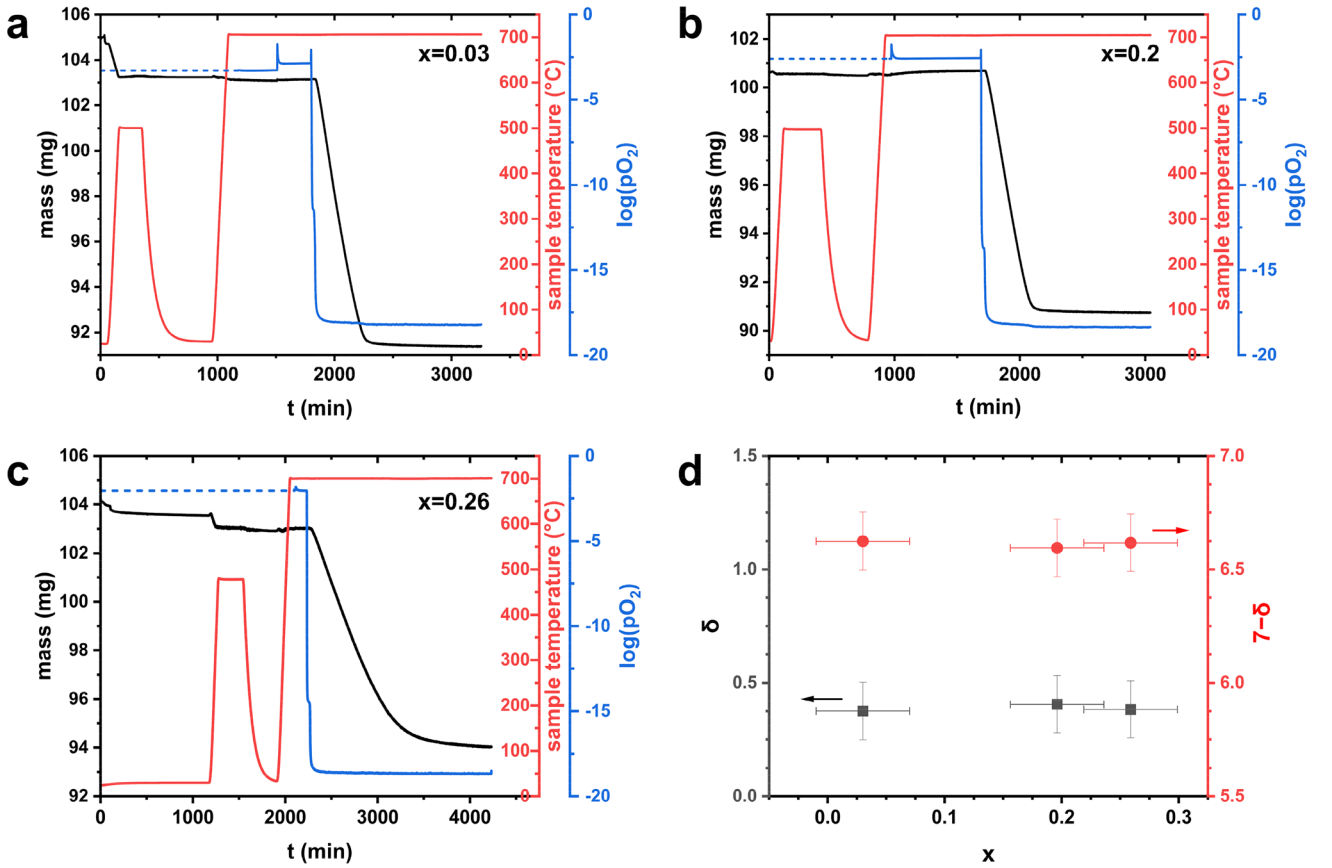

Figure 7. TGA decomposition study to determine the average room-temperature oxygen substoichiometry (δ) of $Y_2(Y_xRu_{1-x})_2O_{7-\delta}$ electrocatalysts, where x is equal to (a) 0.03, (b) 0.2, and (c) 0.26. (d) Average room-temperature, as-prepared oxygen stoichiometry as a function of the amount of Y substitution at the B-site.

The oxygen stoichiometry was determined by comparing the mass of dried pyrochlore powder with that of the Ru and Y_2O_3 mixture after the decomposition step in $H_2/H_2O/Ar$ at 700 °C, accounting for the buoyancy and any hydration effects. The oxygen stoichiometry of $Y_2(Y_xRu_{1-x})_2O_{7-\delta}$ is determined using the corrected values based on the following equations:

$$n_{YRO} = \frac{m_d - m_{setup}}{(1+x)M_{Y_2O_3} + (2-2x)M_{Ru}} \quad (5)$$

$$\delta = 4 - 3x - \frac{m_{o,d} + m_{setup} - m_d}{M_O \times n_{YRO}} \quad (6)$$

where n_{YRO} is the amount of $Y_2(Y_xRu_{1-x})_2O_{7-\delta}$ powder (mmol), m_d is the mass (mg) after the decomposition, M_{Y2O3} is the molar mass of Y_2O_3 (225.81 g/mol), M_{Ru} is the molar mass of Ru (101.07 g/mol), x is the Y dopant ratio, x in $Y_2(Y_xRu_{1-x})_2O_{7-\delta}$, δ is the average oxygen nonstoichiometry of $Y_2(Y_xRu_{1-x})_2O_{7-\delta}$, $m_{o,d}$ is the dried powder mass before the decomposition at room temperature, m_{setup} is the mass change from the setup of the instrument, including buoyancy and proton uptake effects, and M_O is the molar mass of oxygen (15.999 g/mol). From the measured reduction in mass due to the oxygen loss during the decomposition step, the initial average oxygen stoichiometries at room temperature in the three pyrochlore samples were calculated to be $Y_2(Y_{0.03}Ru_{0.97})_2O_{6.62}$, $Y_2(Y_{0.2}Ru_{0.8})_2O_{6.59}$, and $Y_2(Y_{0.3}Ru_{0.7})_2O_{6.62}$ (Figure 7d). In this setup, the mass change due to oxygen loss can be very precisely determined. The large error bars on delta are due to the uncertainty of the cation composition determined by XRF (±2% uncertainty in Y and Ru content).

Our results indicate that although these $Y_2(Y_xRu_{1-x})_2O_{7-\delta}$ electrocatalysts are all significantly oxygen deficient, the concentration of oxygen vacancies is already high at $x = 0.03$ and does not increase with the further addition of Y to the B-site. This consistent oxygen stoichiometry as Y is increasingly substituted at the B-site suggests that the Y'_{Ru} acceptors are primarily electronically compensated, e.g., with Ru^{5+} as $Ru^{\bullet}_{Ru}$, as supported by XPS and EPR results, not ionically by oxygen vacancies, $v^{\bullet\bullet}_O$. Additionally, the degree of average oxygen substoichiometry is much higher than the amount expected from pure ionic compensation of Y alone. The oxygen deficiency indicates the presence of other acceptors or structural vacancies in a defect-ordered structure. These oxygen vacancies should greatly affect the active sites for OER and alter the adsorption and desorption mechanisms between electrocatalysts, reactants, and intermediates, through the changes in the bulk properties, such as electronic structure and conductivity, and thus the improvement of charge transfer kinetics.[56,74]

The excess of trivalent Y, which substitutes for tetravalent Ru, corresponds to acceptor doping. This doping can be compensated in different ways, either ionically, as in Y-stabilized ZrO_2, or electronically. The latter can be achieved either by removing an electron from the valence band, i.e., by moving the Fermi energy into the valence band (rigid band model), or by trapping of holes on either oxygen or ruthenium

https://doi.org/10.1021/jacs.4c04292
J. Am. Chem. Soc. 2024, 146, 18524−18534

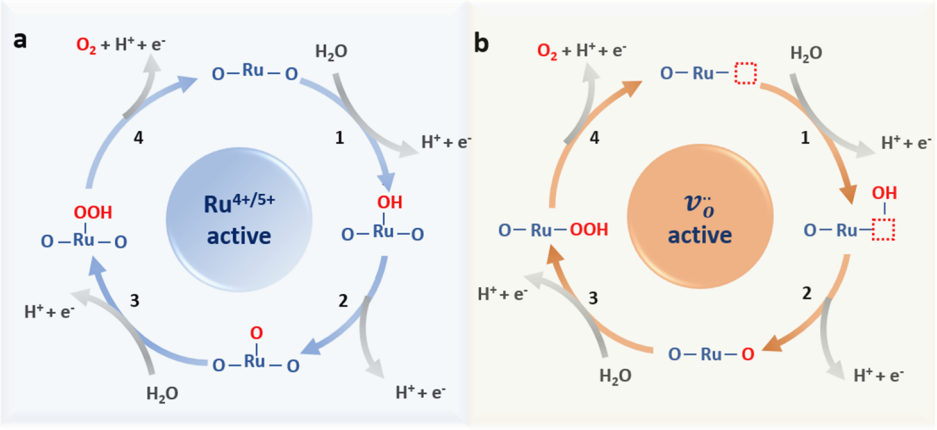

Figure 8. Illustrations of (a) $Ru^{4+/5+}$ and (b) the lattice oxygen vacancy as activation structures for the OER activity of defect-engineered $Y_2(Y_xRu_{1-x})_2O_{7-\delta}$ electrocatalysts.

(hole polaron formation). Our XPS valence band and Ru 3d data clearly reveal that the compensation of the acceptors is achieved by partial oxidation of Ru from 4+ to 5+. As the high binding energy shoulder of the O 1s emission also increases slightly with increasing Y content, some hole trapping on O may also contribute to charge compensation. Consistently, the TGA data reveal no increase in oxygen vacancy concentration with increasing Y amount, further providing support of the electronic rather than ionic compensation in this series. High valence states of Ru may give rise to enhanced catalytic activity through promoting charge transfer between O 2p and Ru 4d bands.[46] Previously, mixed valence oxides were observed in $MnO_{2-\delta}$ (Mn^{3+}/Mn^{4+}), which show higher catalytic activity than its single valence oxide counterparts.[75,76] Similarly, defect engineering of Ru^{4+} and Ru^{5+} oxidation states could be an effective way to create the optimized compositions for $Y_2(Y_xRu_{1-x})_2O_{7-\delta}$ to have a high activity. The mixed valences associated oxygen defects were indeed shown to play significant roles in OER.[56,77] Our convergent structure–property relationship studies indicate the coexistence of Ru^{4+} and Ru^{5+} in $Y_2(Y_xRu_{1-x})_2O_{7-\delta}$ favors the overall OER that involves both $Ru^{4+/5+}$ active and oxygen defect active sites (Figure 8). We hypothesize that the existence of multiple valences in Ru cations provides more than one advantage, as the OER involves the exchange of "O^-" anions through the reaction with redox couple of Ru^{4+}/Ru^{5+}: $Ru^{5+} + O^{2-} \leftrightarrow Ru^{4+} + O^-$ (Figure 8a). The existence of these two valence stages at the optimal overall compositions results in band energy and overall composition stability due to the dynamic nature of the OER process.[78] Our valence band study indicates that the optimal band center is about 1.27 eV below the Fermi level. In addition, a mixed valence compound contains a higher number of oxygen defects in the catalysts, as shown in our oxygen stoichiometry analysis of these $Y_2(Y_xRu_{1-x})_2O_{7-\delta}$ electrocatalysts (Figure 7). The high level of oxygen defects provides abundant $v_O^{\bullet\bullet}$ sites for intermediates in all three defect-engineered $Y_2(Y_xRu_{1-x})_2O_{6.6}$ pyrochlores for promoting the lattice oxygen mechanism (LOM)[79] and favored electrophilicity for proton release and hydroxyl oxidization (Figure 8b).[48,80]

CONCLUSION

The relationship between key structure factors (i.e., valence, electronic band center and oxygen vacancy) and OER catalytic performance of the OER is often complex and interdependent, which is challenging for obtaining viable design parameters using computer simulation tools. It is particularly difficult to examine the complex oxides with varied and coexisting valence states that are now experimentally observed in electrochemical processes, including the OER reactivity. Using a defect-engineering approach, we experimentally uncovered the optimal compositions through controlled site mixing and studies of the structure–property relationship, particularly detailed valence band and oxygen defect chemistry analyses. The presence of higher valence cations (i.e., Ru^{5+}) impacts the electronic structures, influencing the catalytic activity. Experimentally, the optimal OER performance for the B-site, defect-engineered pyrochlore yttrium ruthenate system can be designed, and $Y_2(Y_{0.2}Ru_{0.8})_2O_{6.6}$, which has a valence band center at ~1.27 eV below the Fermi level, was found to be the most active OER catalyst with a good stability. This study points to an effective synthetic strategy to experimentally design and identify the optimal composition of OER electrocatalysts by modulating active site oxidation state, oxygen vacancy, and band center position.

ASSOCIATED CONTENT

Supporting Information

The Supporting Information is available free of charge at https://pubs.acs.org/doi/10.1021/jacs.4c04292.

Information on chemicals used, Rietveld refinement data, SEM, TEM, Tafel plot, stability data, ECSA, XPS, XRD after TGA decomposition study, XRF, and EIS data (PDF)

AUTHOR INFORMATION

Corresponding Author

Hong Yang – *Department of Chemical and Biomolecular Engineering, University of Illinois Urbana–Champaign, Urbana, Illinois 61801, United States; Materials Research Laboratory, University of Illinois Urbana–Champaign, Urbana, Illinois 61801, United States;* orcid.org/0000-0003-3459-4516; Email: hy66@illinois.edu

Authors

Bidipta Ghosh – *Department of Chemical and Biomolecular Engineering, University of Illinois Urbana–Champaign, Urbana, Illinois 61801, United States*

https://doi.org/10.1021/jacs.4c04292
J. Am. Chem. Soc. 2024, 146, 18524–18534

Cheng Zhang − *Department of Chemical and Biomolecular Engineering, University of Illinois Urbana−Champaign, Urbana, Illinois 61801, United States*
Stefanie Frick − *Department of Electronic Structure of Materials, Institute of Materials Science, Technical University of Darmstadt, Darmstadt, Germany 64287*
En Ju Cho − *Department of Materials Science and Engineering, University of Illinois Urbana−Champaign, Urbana, Illinois 61801, United States; Materials Research Laboratory, University of Illinois Urbana−Champaign, Urbana, Illinois 61801, United States*
Toby Woods − *Center of Research and Educational Support, X-ray Diffraction Laboratory, School of Chemical Sciences, University of Illinois Urbana−Champaign, Urbana, Illinois 61801, United States;* orcid.org/0000-0002-1737-811X
Yujie Yang − *Department of Chemical and Biomolecular Engineering, University of Illinois Urbana−Champaign, Urbana, Illinois 61801, United States*
Nicola H. Perry − *Department of Materials Science and Engineering, University of Illinois Urbana−Champaign, Urbana, Illinois 61801, United States; Materials Research Laboratory, University of Illinois Urbana−Champaign, Urbana, Illinois 61801, United States;* orcid.org/0000-0002-7207-2113
Andreas Klein − *Department of Electronic Structure of Materials, Institute of Materials Science, Technical University of Darmstadt, Darmstadt, Germany 64287*

Complete contact information is available at: https://pubs.acs.org/10.1021/jacs.4c04292

Notes

The authors declare no competing financial interest.

■ ACKNOWLEDGMENTS

This work was supported by U.S. National Science Foundation (CBET-2055734) and Deutsche Forschungsgemeinschaft (DFG, KL1225/11-1). The EM characterizations were carried out at the Illinois Materials Research Laboratory Central Facilities. The X-ray diffraction was carried out at the George L. Clark X-ray Facility and 3M Materials Laboratory, School of Chemical Science at UIUC.

■ REFERENCES

(1) Chatenet, M.; Pollet, B. G.; Dekel, D. R.; Dionigi, F.; Deseure, J.; Millet, P.; Braatz, R. D.; Bazant, M. Z.; Eikerling, M.; Staffell, I.; Balcombe, P.; Shao-Horn, Y.; Schäfer, H. Water electrolysis: From textbook knowledge to the latest scientific strategies and industrial developments. *Chem. Soc. Rev.* **2022**, *51*, 4583−4762.
(2) Song, J.; Wei, C.; Huang, Z.-F.; Liu, C.; Zeng, L.; Wang, X.; Xu, Z. J. A review on fundamentals for designing oxygen evolution electrocatalysts. *Chem. Soc. Rev.* **2020**, *49*, 2196−2214.
(3) Shiva Kumar, S.; Lim, H. An overview of water electrolysis technologies for green hydrogen production. *Energy Rep.* **2022**, *8*, 13793−13813.
(4) Zhang, X.; Shi, C.; Chen, B.; Kuhn, A. N.; Ma, D.; Yang, H. Progress in hydrogen production over transition metal carbide catalysts: Challenges and opportunities. *Curr. Opin. Chem. Eng.* **2018**, *20*, 68−77.
(5) Buttler, A.; Spliethoff, H. Current status of water electrolysis for energy storage, grid balancing and sector coupling via power-to-gas and power-to-liquids: A review. *Renew. Sustain. Energy Rev.* **2018**, *82*, 2440−2454.
(6) Ehlers, J. C.; Feidenhans'l, A. A.; Therkildsen, K. T.; Larrazábal, G. O. Affordable green hydrogen from akaline water electrolysis: Key research needs from an industrial perspective. *ACS Energy Lett.* **2023**, *8*, 1502−1509.
(7) Yu, S.; Yang, H. Design principles for the synthesis of platinum−cobalt intermetallic nanoparticles for electrocatalytic applications. *Chem. Commun.* **2023**, *59*, 4852−4871.
(8) Camargo, P. H. C.; Peng, Z.; Lu, X.; Yang, H.; Xia, Y. Synthesis and application of $RuSe_{2+\delta}$ nanotubes as a methanol tolerant electrocatalyst for the oxygen reduction reaction. *J. Mater. Chem.* **2009**, *19*, 1024−1030.
(9) Yue, M.; Lambert, H.; Pahon, E.; Roche, R.; Jemei, S.; Hissel, D. Hydrogen energy systems: A critical review of technologies, applications, trends and challenges. *Renew. Sustain. Energy Rev.* **2021**, *146*, No. 111180.
(10) Turner, J. A. *A Realizable Renewable Energy Future. Science* **1999**, *285*, 687−689.
(11) Suen, N.-T.; Hung, S.-F.; Quan, Q.; Zhang, N.; Xu, Y.-J.; Chen, H. M. Electrocatalysis for the oxygen evolution reaction: Recent development and future perspectives. *Chem. Soc. Rev.* **2017**, *46*, 337−365.
(12) Wang, S.; Lu, A.; Zhong, C.-J., Hydrogen production from water electrolysis: Role of catalysts. *Nano Converg.* **2021**, No. 4, DOI: 10.1186/s40580-021-00254-x
(13) Pei, Z.; Zhang, H.; Luan, D.; Lou, X. W. D. Electrocatalytic acidic oxygen evolution: From catalyst design to industrial applications. *Matter* **2023**, *6*, 4128−4144.
(14) Carmo, M.; Fritz, D. L.; Mergel, J.; Stolten, D. A comprehensive review on PEM water electrolysis. *Int. J. Hydrogen Energy* **2013**, *38*, 4901−4934.
(15) Wang, T.; Cao, X.; Jiao, L. PEM water electrolysis for hydrogen production: fundamentals, advances, and prospects. *Carbon Neutrality* **2022**, *1* (21), DOI: 10.1007/s43979-022-00022-8
(16) Bonanno, M.; Müller, K.; Bensmann, B.; Hanke-Rauschenbach, R.; Aili, D.; Franken, T.; Chromik, A.; Peach, R.; Freiberg, A. T. S.; Thiele, S., Review and prospects of PEM water electrolysis at elevated temperature operation. *Adv. Mater. Technol.* **2023**, *9*, No. 2300281.
(17) Shiva Kumar, S.; Himabindu, V. Hydrogen production by PEM water electrolysis − A review. *Mater. Sci. Energy Technol.* **2019**, *2*, 442−454.
(18) Reier, T.; Nong, H. N.; Teschner, D.; Schlögl, R.; Strasser, P. Electrocatalytic oxygen evolution reaction in acidic environments − Reaction mechanisms and catalysts. *Adv. Energy Mater.* **2017**, *7*, DOI: 10.1002/aenm.201601275.
(19) Li, L.; Wang, P.; Shao, Q.; Huang, X. Recent progress in advanced electrocatalyst design for acidic oxygen evolution reaction. *Adv. Mater.* **2021**, *33*, 2004243.
(20) Fabbri, E.; Schmidt, T. J. Oxygen evolution reaction—The enigma in water electrolysis. *ACS Catal.* **2018**, *8*, 9765−9774.
(21) Yin, H.; Tang, Z. Ultrathin two-dimensional layered metal hydroxides: an emerging platform for advanced catalysis, energy conversion and storage. *Chem. Soc. Rev.* **2016**, *45*, 4873−4891.
(22) Liu, C.; Qian, J.; Ye, Y.; Zhou, H.; Sun, C.-J.; Sheehan, C.; Zhang, Z.; Wan, G.; Liu, Y.-S.; Guo, J.; Li, S.; Shin, H.; Hwang, S.; Gunnoe, T. B.; Goddard, W. A.; Zhang, S. Oxygen evolution reaction over catalytic single-site Co in a well-defined brookite TiO_2 nanorod surface. *Nat. Catal.* **2021**, *4*, 36−45.
(23) Seitz, L. C.; Dickens, C. F.; Nishio, K.; Hikita, Y.; Montoya, J.; Doyle, A.; Kirk, C.; Vojvodic, A.; Hwang, H. Y.; Norskov, J. K.; Jaramillo, T. F. A highly active and stable $IrO_x/SrIrO_3$ catalyst for the oxygen evolution reaction. *Science* **2016**, *353*, 1011−1014.
(24) Seh, Z. W.; Kibsgaard, J.; Dickens, C. F.; Chorkendorff, I.; Nørskov, J. K.; Jaramillo, T. F. Combining theory and experiment in electrocatalysis: Insights into materials design. *Science* **2017**, *355*, DOI: 10.1126/science.aad4998.
(25) Zhang, B.; Zheng, X.; Voznyy, O.; Comin, R.; Bajdich, M.; García-Melchor, M.; Han, L.; Xu, J.; Liu, M.; Zheng, L.; García de Arquer, F. P.; Dinh, C. T.; Fan, F.; Yuan, M.; Yassitepe, E.; Chen, N.; Regier, T.; Liu, P.; Li, Y.; De Luna, P.; Janmohamed, A.; Xin, H. L.; Yang, H.; Vojvodic, A.; Sargent, E. H. Homogeneously dispersed multimetal oxygen-evolving catalysts. *Science* **2016**, *352*, 333−337.

(26) Praneeth, V. K. K.; Kondo, M.; Okamura, M.; Akai, T.; Izu, H.; Masaoka, S. Pentanuclear iron catalysts for water oxidation: Substituents provide two routes to control onset potentials. *Chem. Sci.* **2019**, *10*, 4628−4639.
(27) Park, S.; Shao, Y.; Liu, J.; Wang, Y. Oxygen electrocatalysts for water electrolyzers and reversible fuel cells: Status and perspective. *Energy Environ. Sci.* **2012**, *5*, 9331−9344.
(28) Hocking, R. K.; Brimblecombe, R.; Chang, L.-Y.; Singh, A.; Cheah, M. H.; Glover, C.; Casey, W. H.; Spiccia, L. Water-oxidation catalysis by manganese in a geochemical-like cycle. *Nat. Chem.* **2011**, *3*, 461−466.
(29) Hu, H.; Guan, B.; Xia, B.; Lou, X. W. Designed formation of Co_3O_4/$NiCo_2O_4$ double-shelled nanocages with enhanced pseudocapacitive and electrocatalytic properties. *J. Am. Chem. Soc.* **2015**, *137*, 5590−5595.
(30) Zhang, J.; Zhao, Z.; Xia, Z.; Dai, L. A metal-free bifunctional electrocatalyst for oxygen reduction and oxygen evolution reactions. *Nat. Nanotechnol.* **2015**, *10*, 444−452.
(31) Tahir, M.; Pan, L.; Idrees, F.; Zhang, X.; Wang, L.; Zou, J.-J.; Wang, Z. L. Electrocatalytic oxygen evolution reaction for energy conversion and storage: A comprehensive review. *Nano Energy* **2017**, *37*, 136−157.
(32) Raveendran, A.; Chandran, M.; Dhanusuraman, R. A comprehensive review on the electrochemical parameters and recent material development of electrochemical water splitting electrocatalysts. *RSC Adv.* **2023**, *13*, 3843−3876.
(33) Lei, Z.; Wang, T.; Zhao, B.; Cai, W.; Liu, Y.; Jiao, S.; Li, Q.; Cao, R.; Liu, M. Recent progress in electrocatalysts for acidic water oxidation. *Adv. Energy Mater.* **2020**, *10*, DOI: 10.1002/aenm.202000478.
(34) Lee, Y.; Suntivich, J.; May, K. J.; Perry, E. E.; Shao-Horn, Y. Synthesis and activities of rutile IrO_2 and RuO_2 nanoparticles for oxygen evolution in acid and alkaline solutions. *J. Phys. Chem. Lett.* **2012**, *3*, 399−404.
(35) She, L.; Zhao, G.; Ma, T.; Chen, J.; Sun, W.; Pan, H. On the durability of iridium-based electrocatalysts toward the oxygen evolution reaction under acid environment. *Adv. Funct. Mater.* **2022**, *32*, DOI: 10.1002/adfm.202108465.
(36) Shih, P.-C.; Zhang, C.; Raheja, H.; Sun, C.-J.; Yang, H. Polymer entrapment flash pyrolysis for the preparation of nanoscale iridium-free oxygen evolution electrocatalysts. *ChemNanoMat* **2020**, *6*, 930−936.
(37) Li, Y.; Sun, Y.; Qin, Y.; Zhang, W.; Wang, L.; Luo, M.; Yang, H.; Guo, S. Recent advances on water-splitting electrocatalysis mediated by noble-metal-based nanostructured materials. *Adv. Energy Mater.* **2020**, *10*, No. 1903120.
(38) Ying, J.; Chen, J.-B.; Xiao, Y.-X.; Cordoba de Torresi, S. I.; Ozoemena, K. I.; Yang, X.-Y. Recent advances in Ru-based electrocatalysts for oxygen evolution reaction. *J. Mater. Chem. A* **2023**, *11*, 1634−1650.
(39) Zhu, Y. P.; Guo, C.; Zheng, Y.; Qiao, S.-Z. Surface and interface engineering of noble-metal-free electrocatalysts for efficient energy conversion processes. *Acc. Chem. Res.* **2017**, *50*, 915−923.
(40) You, H.; Yang, S.; Ding, B.; Yang, H. Synthesis of colloidal metal and metal alloy nanoparticles for electrochemical energy applications. *Chem. Soc. Rev.* **2013**, *42*, 2880−2904.
(41) Kim, J.; Shih, P.-C.; Tsao, K.-C.; Pan, Y.-T.; Yin, X.; Sun, C.-J.; Yang, H. High-performance pyrochlore-type yttrium ruthenate electrocatalyst for oxygen evolution reaction in acidic media. *J. Am. Chem. Soc.* **2017**, *139*, 12076−12083.
(42) Li, A.; Kong, S.; Guo, C.; Ooka, H.; Adachi, K.; Hashizume, D.; Jiang, Q.; Han, H.; Xiao, J.; Nakamura, R. Enhancing the stability of cobalt spinel oxide towards sustainable oxygen evolution in acid. *Nat. Catal.* **2022**, *5*, 109−118.
(43) Chong, L.; Gao, G.; Wen, J.; Li, H.; Xu, H.; Green, Z.; Sugar, J. D.; Kropf, A. J.; Xu, W.; Lin, X.-M.; Xu, H.; Wang, L.-W.; Liu, D.-J. La- and Mn-doped cobalt spinel oxygen evolution catalyst for proton exchange membrane electrolysis. *Science* **2023**, *380*, 609−616.
(44) Kim, M.; Park, J.; Kang, M.; Kim, J. Y.; Lee, S. W. Toward efficient electrocatalytic oxygen evolution: Emerging opportunities with metallic pyrochlore oxides for electrocatalysts and conductive supports. *ACS Cent. Sci.* **2020**, *6*, 880−891.
(45) Gayen, P.; Saha, S.; Ramani, V. Pyrochlores for advanced oxygen electrocatalysis. *Acc. Chem. Res.* **2022**, *55*, 2191−2200.
(46) Wang, H.; Zhai, T.; Wu, Y.; Zhou, T.; Zhou, B.; Shang, C.; Guo, Z. High-valence oxides for high performance oxygen evolution electrocatalysis. *Adv. Sci.* **2023**, *10*, No. 2301706.
(47) Deka, N.; Jones, T. E.; Falling, L. J.; Sandoval-Diaz, L.-E.; Lunkenbein, T.; Velasco-Velez, J.-J.; Chan, T.-S.; Chuang, C.-H.; Knop-Gericke, A.; Mom, R. V. On the operando structure of ruthenium oxides during the oxygen evolution reaction in acidic media. *ACS Catal.* **2023**, *13*, 7488−7498.
(48) Retuerto, M.; Pascual, L.; Calle-Vallejo, F.; Ferrer, P.; Gianolio, D.; Pereira, A. G.; García, Á.; Torrero, J.; Fernández-Díaz, M. T.; Bencok, P.; Peña, M. A.; Fierro, J. L. G.; Rojas, S. Na-doped ruthenium perovskite electrocatalysts with improved oxygen evolution activity and durability in acidic media. *Nat. Commun.* **2019**, *10*, DOI: 10.1038/s41467-019-09791-w.
(49) Zhang, C.; Wang, F.; Xiong, B.; Yang, H. Regulating the electronic structures of mixed B-site pyrochlore to enhance the turnover frequency in water oxidation. *Nano Converg.* **2022**, *9*, DOI: 10.1186/s40580-022-00311-z.
(50) Yan, X.; Jia, Y.; Yao, X. Defects on carbons for electrocatalytic oxygen reduction. *Chem. Soc. Rev.* **2018**, *47*, 7628−7658.
(51) Jia, Y.; Jiang, K.; Wang, H.; Yao, X. The role of defect sites in nanomaterials for electrocatalytic energy conversion. *Chem.* **2019**, *5*, 1371−1397.
(52) Liu, J.; Zheng, M.; Li, J.; Yuan, Y.; Li, C.; Zhang, S.; Yang, L.; Bai, Z.; Lu, J. Lithiation-induced defect engineering to promote oxygen evolution reaction. *Adv. Funct. Mater.* **2023**, *33*, No. 2209753.
(53) Paier, J.; Penschke, C.; Sauer, J. Oxygen defects and surface chemistry of ceria: Quantum chemical studies compared to experiment. *Chem. Rev.* **2013**, *113*, 3949−3985.
(54) Li, G.; Blake, G. R.; Palstra, T. T. M. Vacancies in functional materials for clean energy storage and harvesting: the perfect imperfection. *Chem. Soc. Rev.* **2017**, *46*, 1693−1706.
(55) Zhang, N.; Wang, C.; Chen, J.; Hu, C.; Ma, J.; Deng, X.; Qiu, B.; Cai, L.; Xiong, Y.; Chai, Y. Metal substitution steering electron correlations in pyrochlore ruthenates for efficient acidic water oxidation. *ACS Nano* **2021**, *15*, 8537−8548.
(56) Zhu, K.; Shi, F.; Zhu, X.; Yang, W. The roles of oxygen vacancies in electrocatalytic oxygen evolution reaction. *Nano Energy* **2020**, *73*, 104761.
(57) Arandiyan, H.; Mofarah, S. S.; Wang, Y.; Cazorla, C.; Jampaiah, D.; Garbrecht, M.; Wilson, K.; Lee, A. F.; Zhao, C.; Maschmeyer, T. Impact of surface defects on $LaNiO_3$ perovskite electrocatalysts for the oxygen evolution reaction. *Chem.—Eur. J.* **2021**, *27*, 14418−14426.
(58) Jin, X.; Lee, T.; Tamakloe, W.; Patil, S. B.; Soon, A.; Kang, Y.-M.; Hwang, S.-J. In situ defect engineering route to optimize the cationic redox activity of layered double hydroxide nanosheet via strong electronic coupling with holey substrate. *Adv. Sci.* **2022**, *9*, DOI: 10.1002/advs.202103368.
(59) Arandiyan, H.; Mofarah, S. S.; Sorrell, C. C.; Doustkhah, E.; Sajjadi, B.; Hao, D.; Wang, Y.; Sun, H.; Ni, B.-J.; Rezaei, M.; Shao, Z.; Maschmeyer, T. Defect engineering of oxide perovskites for catalysis and energy storage: Synthesis of chemistry and materials science. *Chem. Soc. Rev.* **2021**, *50*, 10116−10211.
(60) Kim, J.; Yin, X.; Tsao, K.-C.; Fang, S.; Yang, H. $Ca_2Mn_2O_5$ as oxygen-deficient perovskite electrocatalyst for oxygen evolution reaction. *J. Am. Chem. Soc.* **2014**, *136*, 14646−14649.
(61) Zhu, Y.; Liu, X.; Jin, S.; Chen, H.; Lee, W.; Liu, M.; Chen, Y. Anionic defect engineering of transition metal oxides for oxygen reduction and evolution reactions. *J. Mater. Chem.* **2019**, *7*, 5875−5897.
(62) Levin, N.; Casadevall, C.; Cutsail Iii, G. E.; Lloret-Fillol, J.; DeBeer, S.; Rüdiger, O. XAS and EPR in situ observation of Ru(V)

oxo intermediate in a Ru water oxidation complex. *ChemElectroChem.* **2022**, *9*, DOI: 10.1002/celc.202101683.
(63) Feng, Q.; Wang, Q.; Zhang, Z.; Xiong, Y.; Li, H.; Yao, Y.; Yuan, X.-Z.; Williams, M. C.; Gu, M.; Chen, H.; Li, H.; Wang, H. Highly active and stable ruthenate pyrochlore for enhanced oxygen evolution reaction in acidic medium electrolysis. *Appl. Catal., B* **2019**, *244*, 494−501.
(64) Han, T.; Wu, J.; Lu, X.; Wang, Y.; Zhao, H.; Tang, X. Study of OER electrocatalysts performance of Fe/Mn doped pyrochlorestructure. *J. Solid State Chem.* **2021**, *303*, 122457.
(65) Chen, S.; Huang, H.; Jiang, P.; Yang, K.; Diao, J.; Gong, S.; Liu, S.; Huang, M.; Wang, H.; Chen, Q. Mn-doped RuO_2 nanocrystals as highly active electrocatalysts for enhanced oxygen evolution in acidic media. *ACS Catal.* **2020**, *10*, 1152−1160.
(66) Li, H.; Li, B.; Zou, Y.; Xiang, C.; Zhang, H.; Xu, F.; Sun, L.; He, K. Modulating valence band to enhance the catalytic activity of Co-Cr-B/NG for hydrolysis of sodium borohydride. *J. Alloys Compd.* **2022**, *924*, 166556.
(67) Pan, Y.; Sun, K.; Lin, Y.; Cao, X.; Cheng, Y.; Liu, S.; Zeng, L.; Cheong, W.-C.; Zhao, D.; Wu, K.; Liu, Z.; Liu, Y.; Wang, D.; Peng, Q.; Chen, C.; Li, Y. Electronic structure and d-band center control engineering over M-doped CoP (M = Ni, Mn, Fe) hollow polyhedron frames for boosting hydrogen production. *Nano Energy* **2019**, *56*, 411−419.
(68) Hu, J.; Al-Salihy, A.; Zhang, B.; Li, S.; Xu, P. Mastering the d-band center of iron-series metal-based electrocatalysts for enhanced electrocatalytic water splitting. *Int. J. Mol. Sci.* **2022**, *23*,.
(69) Nilsson, A.; Pettersson, L. G. M.; Hammer, B.; Bligaard, T.; Christensen, C. H.; Nørskov, J. K. The electronic structure effect in heterogeneous catalysis. *Catal. Lett.* **2005**, *100*, 111−114.
(70) Nørskov, J. K.; Abild-Pedersen, F.; Studt, F.; Bligaard, T. Density functional theory in surface chemistry and catalysis. *Proc. Natl. Acad. Sci. U. S. A.* **2011**, *108*, 937−943.
(71) Hu, Q.; Gao, K.; Wang, X.; Zheng, H.; Cao, J.; Mi, L.; Huo, Q.; Yang, H.; Liu, J.; He, C. Subnanometric Ru clusters with upshifted D band center improve performance for alkaline hydrogen evolution reaction. *Nat. Commun.* **2022**, *13*, No. 3958.
(72) Djurovic, D.; Zinkevich, M.; Aldinger, F. Thermodynamic modeling of the yttrium−oxygen system. *Calphad* **2007**, *31*, 560−566.
(73) Chatillon, C.; Nuta, I.; Roki, F.-Z.; Fischer, E. Chemical thermodynamics of RuO_2(s). *J. Nucl. Mater.* **2018**, *509*, 742−751.
(74) Kim, J.; Chen, X.; Pan, Y.-T.; Shih, P.-C.; Yang, H. W-doped $CaMnO_{2.5}$ and $CaMnO_3$ electrocatalysts for enhanced performance in oxygen evolution and reduction reactions. *J. Electrochem. Soc.* **2017**, *164*, 1074−1080.
(75) Kaur, M.; Chhetri, M.; Rao, C. N. R. Photoelectrochemical OER activity by employing $BiVO_4$ with manganese oxide co-catalysts. *Phys. Chem. Chem. Phys.* **2020**, *22*, 811−817.
(76) Lourenço, A. A.; Silva, V. D.; da Silva, R. B.; Silva, U. C.; Chesman, C.; Salvador, C.; Simões, T. A.; Macedo, D. A.; da Silva, F. F. Metal-organic frameworks as template for synthesis of Mn^{3+}/Mn^{4+} mixed valence manganese cobaltites electrocatalysts for oxygen evolution reaction. *J. Colloid Interface Sci.* **2021**, *582*, 124−136.
(77) Badreldin, A.; Abusrafa, A. E.; Abdel-Wahab, A. Oxygen-deficient cobalt-based oxides for electrocatalytic water splitting. *ChemSusChem* **2021**, *14*, 10−32.
(78) Goodenough, J. B.; Manoharan, R.; Paranthaman, M. Surface protonation and electrochemical activity of oxides in aqueous solution. *J. Am. Chem. Soc.* **1990**, *112*, 2076−2082.
(79) Lee, H. J.; Back, S.; Lee, J. H.; Choi, S. H.; Jung, Y.; Choi, J. W. Mixed transition metal oxide with vacancy-induced lattice distortion for enhanced catalytic activity of oxygen evolution reaction. *ACS Catal.* **2019**, *9*, 7099−7108.
(80) Feng, Q.; Zou, J.; Wang, Y.; Zhao, Z.; Williams, M. C.; Li, H.; Wang, H. Influence of surface oxygen vacancies and ruthenium valence state on the catalysis of pyrochlore oxides. *ACS Appl. Mater. Interfaces* **2020**, *12*, 4520−4530.

https://doi.org/10.1021/jacs.4c04292
J. Am. Chem. Soc. 2024, 146, 18524−18534

Supporting Information

Defect Engineering in Composition and Valence Band Center of $Y_2(Y_xRu_{1-x})_2O_{7-\delta}$ Pyrochlore Electrocatalysts for Oxygen Evolution Reaction

Bidipta Ghosh,[a] Cheng Zhang,[a] Stefanie Frick,[b] En Ju Cho,[c,e] Toby Woods,[d] Yujie Yang,[a]

Nicola Perry,[c,e] Andreas Klein,[b] Hong Yang[a,e,*]

[a] *Department of Chemical and Biomolecular Engineering, University of Illinois at Urbana-Champaign, 600 S. Mathews Avenue, Urbana, Illinois 61801, United States*

[b] *Institute of Materials Science, Technical University of Darmstadt, Otto-Berndt-Str. 3, Darmstadt, Germany, 64287*

[c] *Department of Materials Science and Engineering, University of Illinois at Urbana-Champaign, 1304 W Green Street, Urbana, Illinois 61801, United States*

[d] *Center of Research and Educational Support, X-ray Diffraction Laboratory, School of Chemical Sciences, University of Illinois at Urbana-Champaign, 505 South Mathews Avenue, Urbana, IL 61801, United States*

[e] *Materials Research Laboratory, University of Illinois at Urbana-Champaign, 104 S. Goodwin Ave., Urbana, Illinois 61801, United States*

* Corresponding author: E-mail address: hy66@illinois.edu (H. Yang)

Chemicals

Yttrium (III) nitrate hexahydrate ($Y(NO_3)_3 \cdot 6H_2O$, 99.8%), Ruthenium (III) nitrosyl nitrate solution in dilute nitric acid ($Ru(NO)(NO_3)_x(OH)_y$, 99.9%), Nafion® 117 solution (~5%) were purchased from Sigma-Aldrich. Citric acid monohydrate ($C_6H_8O_7 \cdot H_2O$, 99%) was bought from Fisher Chemical. Veritas® double distilled perchloric acid ($HClO_4$, 70%) was obtained from GFS Chemicals. Tetrahydrofuran (THF) was obtained from Macron Fine Chemicals. Vulcan carbon XC-72 was purchased from Cabot Corporation. Hydrogen (H_2, 99.999%) and oxygen (O_2, 99.999%) were supplied by Airgas, Inc. Carbon paper (Sigracet 29 BC) was purchased from Fuel Cell Store. All chemicals and gases were used without further purification. Deionized (DI) water was obtained after passing through Barnstear E-pure water purification system (18.2 MΩ·cm resistivity, Thermo Fisher Scientific).

Figures

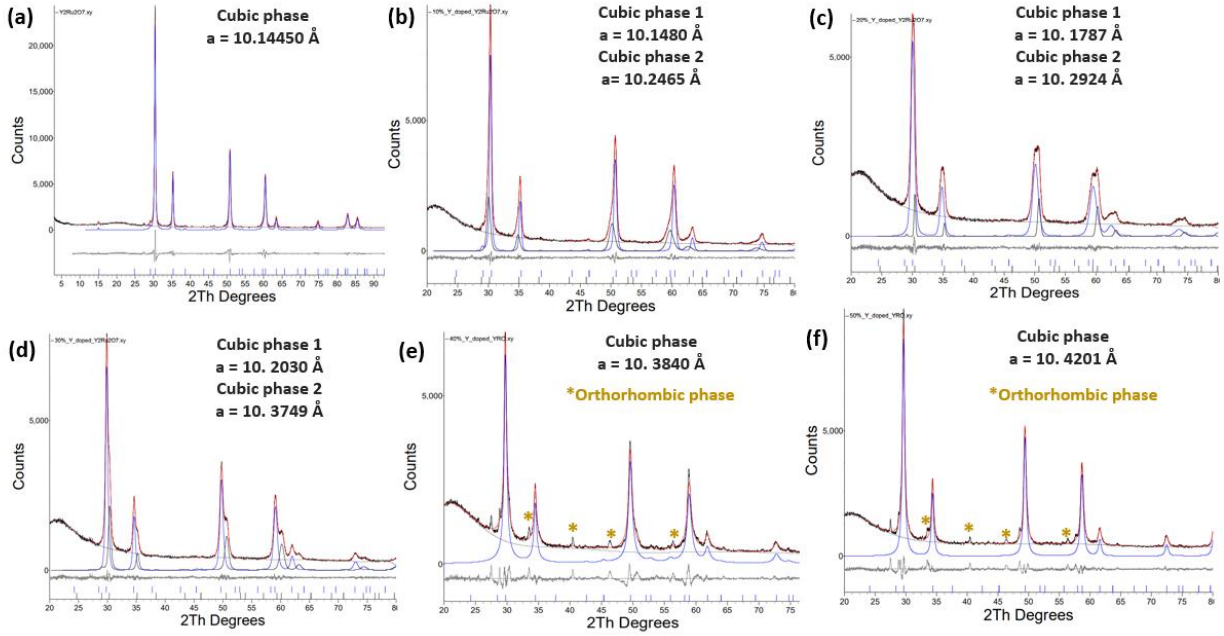

Figure S1. Rietveld refinement of X-ray diffraction patterns of $Y_2(Y_xRu_{1-x})_2O_{7-\delta}$ electrocatalysts with x equal to (a) 0, (b) 0.03, (c) 0.20, (d) 0.26, (e) 0.34, and (f) 0.42, respectively. The red trace is the overall fitted pattern, the black trace is the experimentally recorded pattern, the grey trace is the difference between measured and fitted pattern.

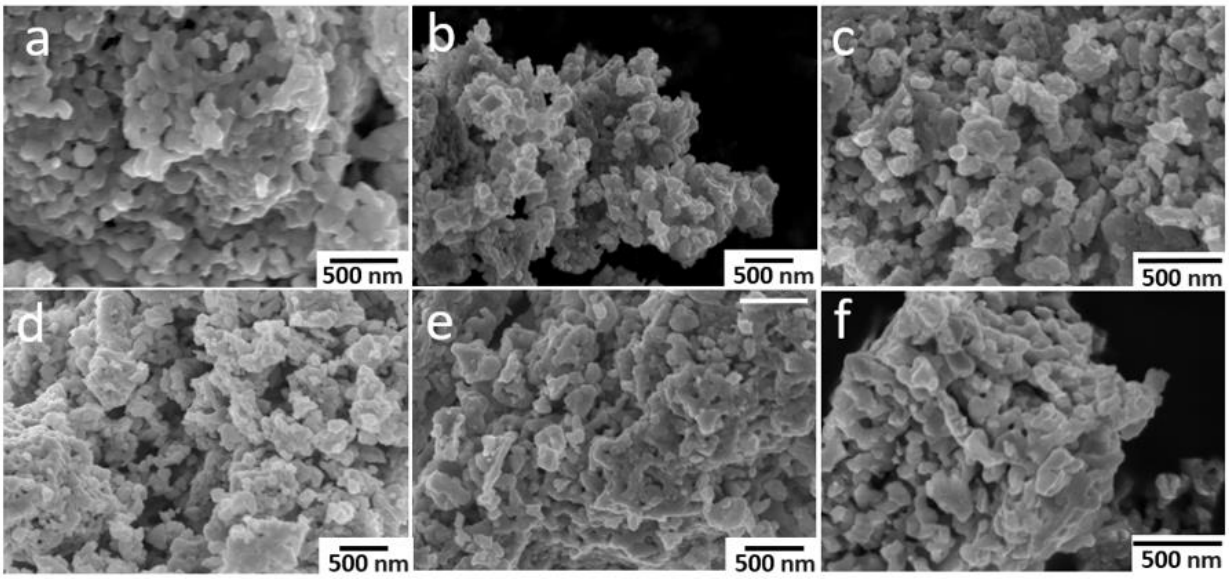

Figure S2. SEM images of $Y_2(Y_xRu_{1-x})_2O_{7-\delta}$ electrocatalysts with x equal to (a) 0, (b) 0.03, (c) 0.20, (d) 0.26, (e) 0.34, and (f) 0.42, respectively.

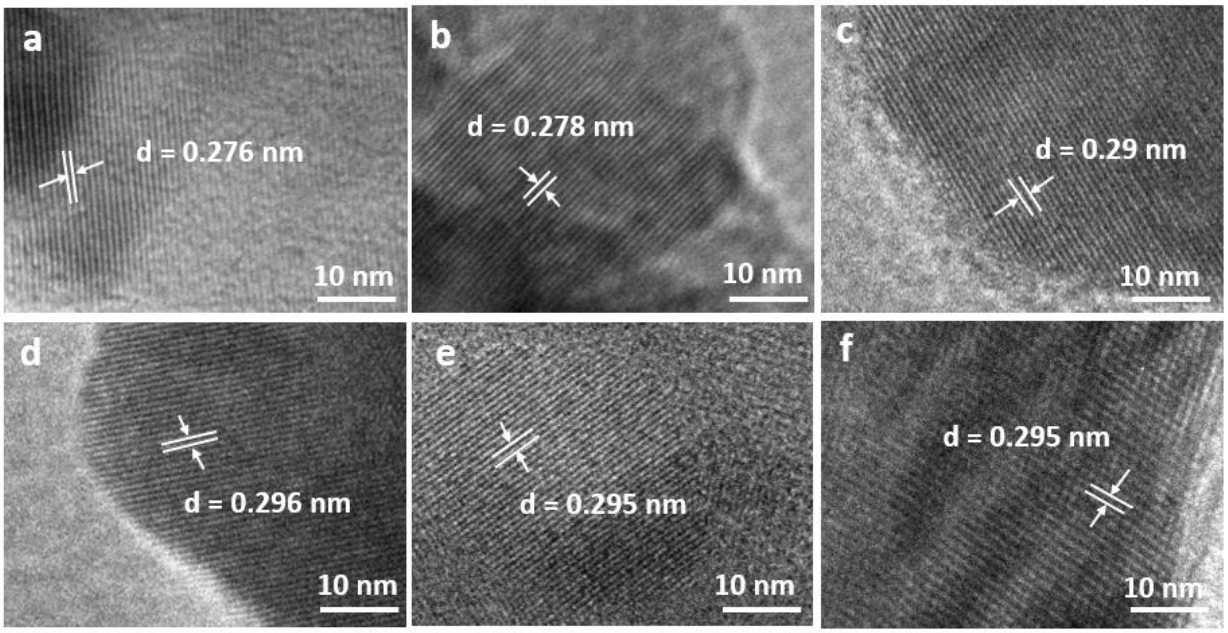

Figure S3. TEM micrographs of $Y_2(Y_xRu_{1-x})_2O_{7-\delta}$ electrocatalysts with x equal to (a) 0, (b) 0.03, (c) 0.20, (d) 0.26, (e) 0.34, and (f) 0.42, respectively.

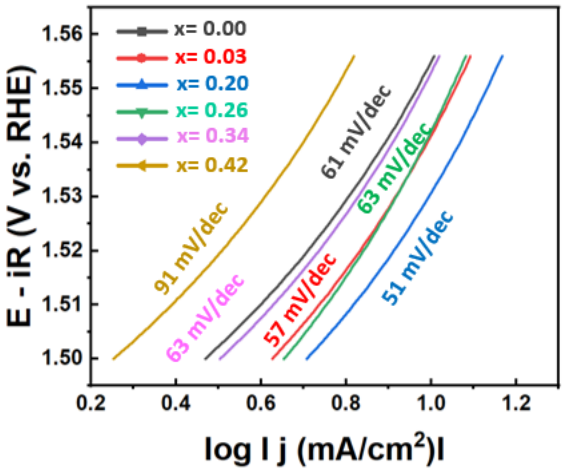

Figure S4. Tafel plot of $Y_2(Y_xRu_{1-x})_2O_{7-\delta}$ electrocatalysts with x equal to (a) 0 (YRO), (b) 0.03, (c) 0.20, (d) 0.26, (e) 0.34, and (f) 0.42, respectively.

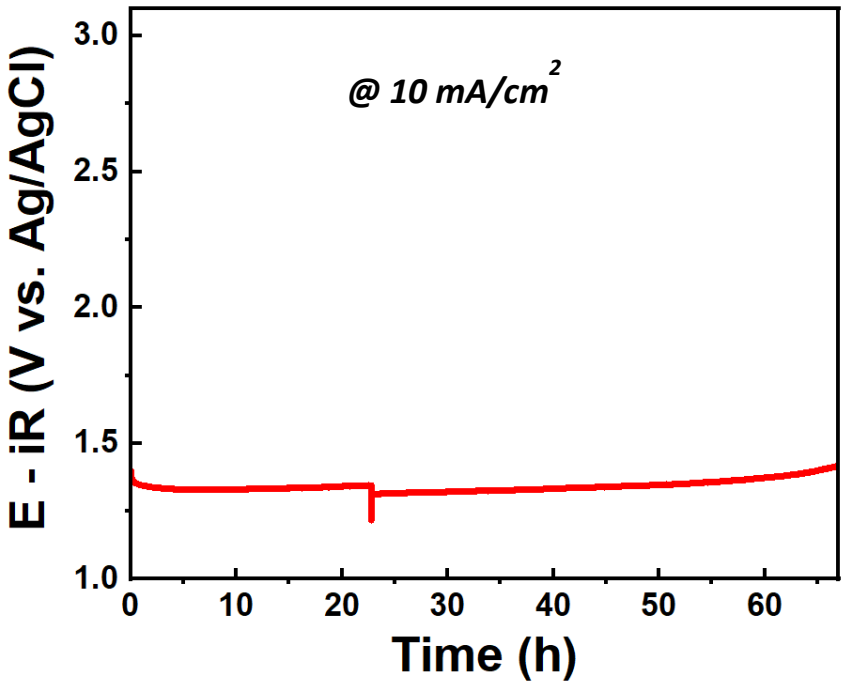

Figure S5. Chronopotentiometric analysis of $Y_2(Y_{0.2}Ru_{0.8})_2O_{7-\delta}$ electrocatalysts in 0.1 M $HClO_4$ on carbon paper, exhibiting a stable potential over 60 h. The dip in the plot indicates the change of electrolyte.

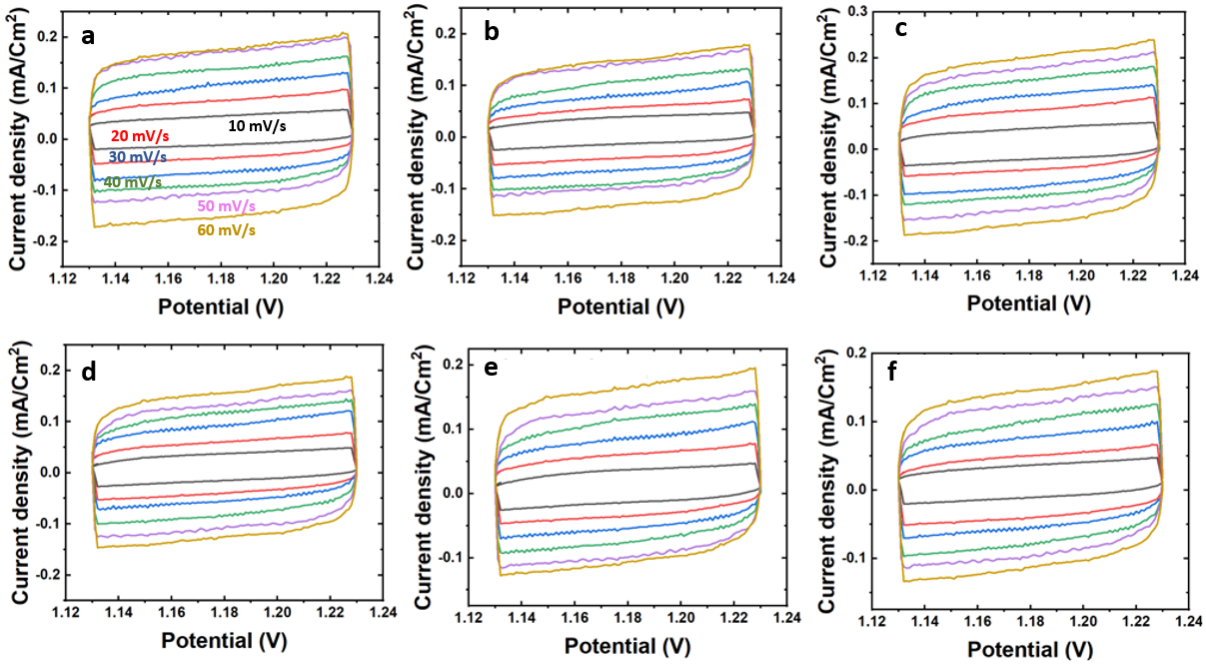

Figure S6. CV curves of $Y_2(Y_xRu_{1-x})_2O_{7-\delta}$ electrocatalysts in 0.1 M $HClO_4$ in the potential range of 1.13–1.23 V vs. RHE at a scan rate of 10, 20, 30, 40, 50 and 60 mV s^{-1}, respectively. The subscript of x is (a) 0 ($Y_2Ru_2O_{7-\delta}$), (b) 0.03, (c) 0.20, (d) 0.26, (e) 0.34, and (f) 0.42, respectively. The color codes of scan rate are the same for all panels.

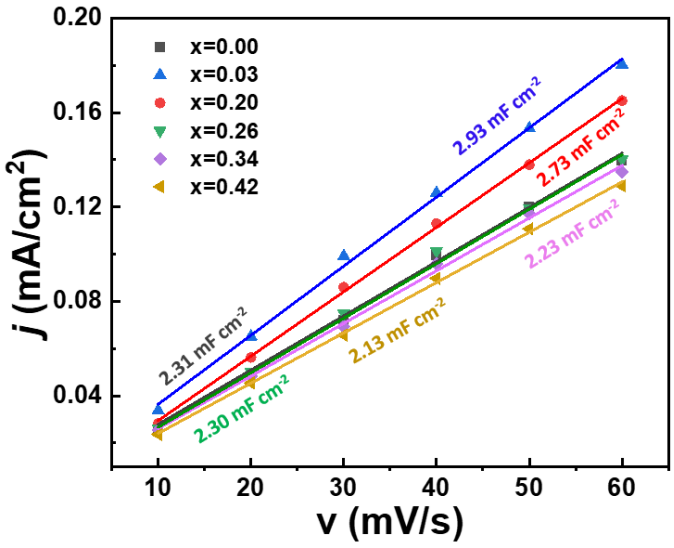

Figure S7. Plot of current density differences (Δj/2) vs. scan rate at 1.18 V vs. RHE of $Y_2(Y_xRu_{1-x})_2O_{7-\delta}$ electrocatalysts. The double-layer capacitance C_{dl} is equivalent to the slope.

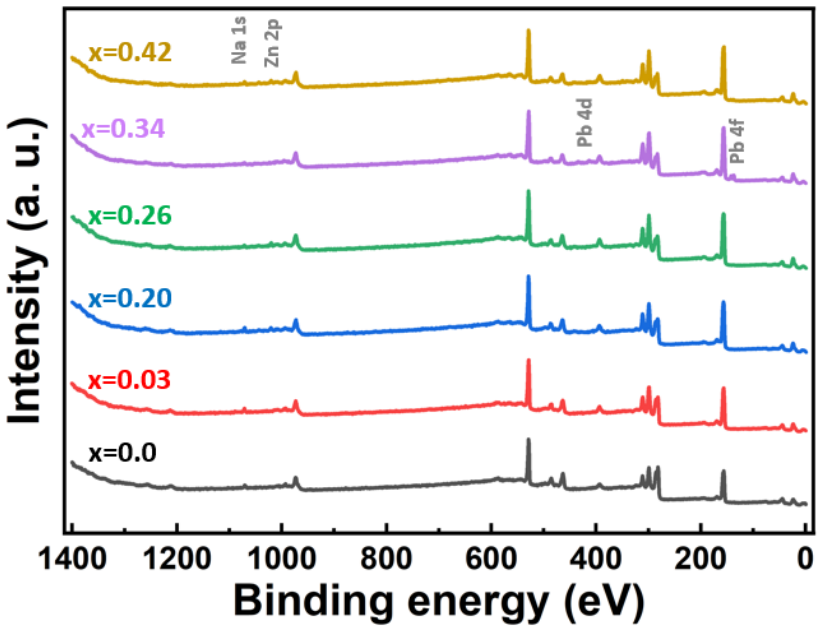

Figure S8. XPS survey scans of $Y_2(Y_xRu_{1-x})_2O_{7-\delta}$ electrocatalysts. Weak Na, Zn and Pb signals were detected in the specimen, which do not affect the analysis of Ru and Y cations.

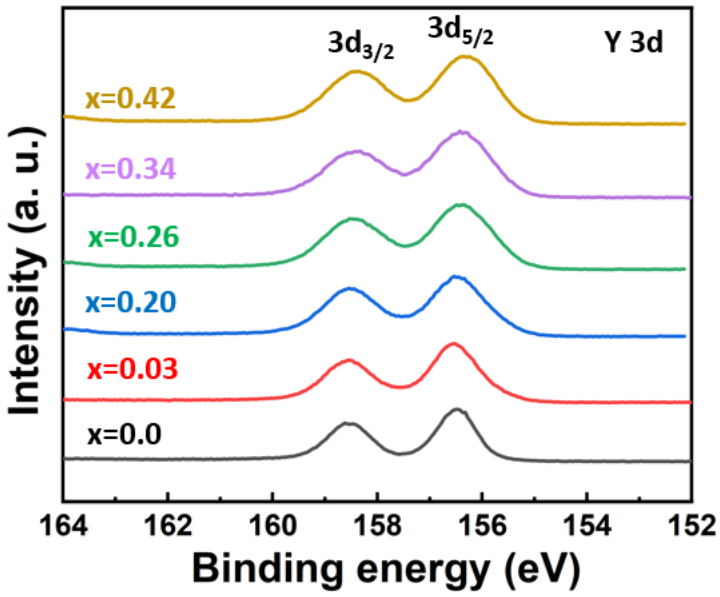

Figure S9. XPS spectra in the Y 3d region of $Y_2(Y_xRu_{1-x})_2O_{7-\delta}$ electrocatalysts.

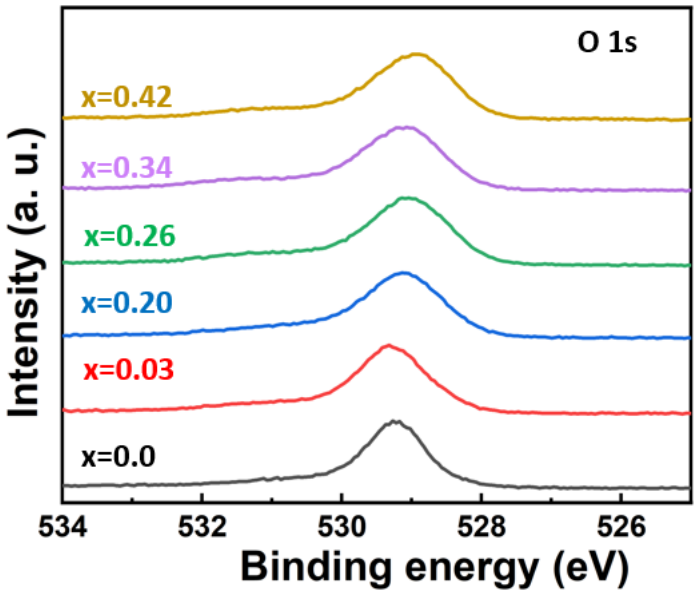

Figure S10. XPS spectra in the O 1s region of $Y_2(Y_xRu_{1-x})_2O_{7-\delta}$ electrocatalysts.

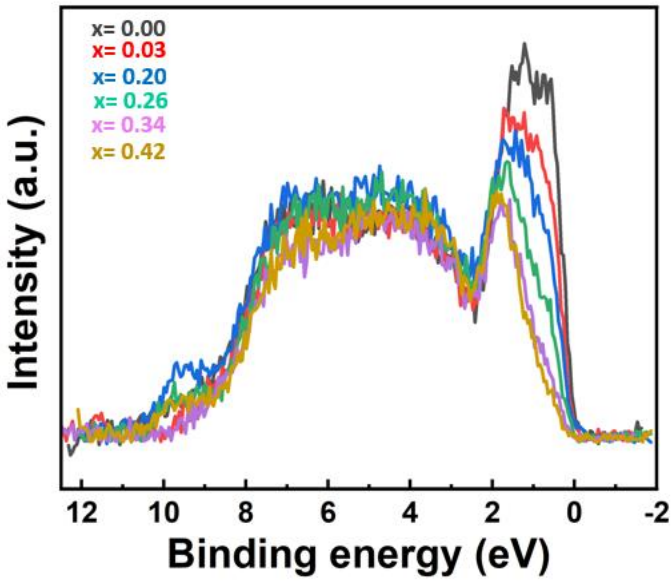

Figure S11. Raw spectra of valence bands for $Y_2(Y_xRu_{1-x})_2O_{7-\delta}$ electrocatalysts.

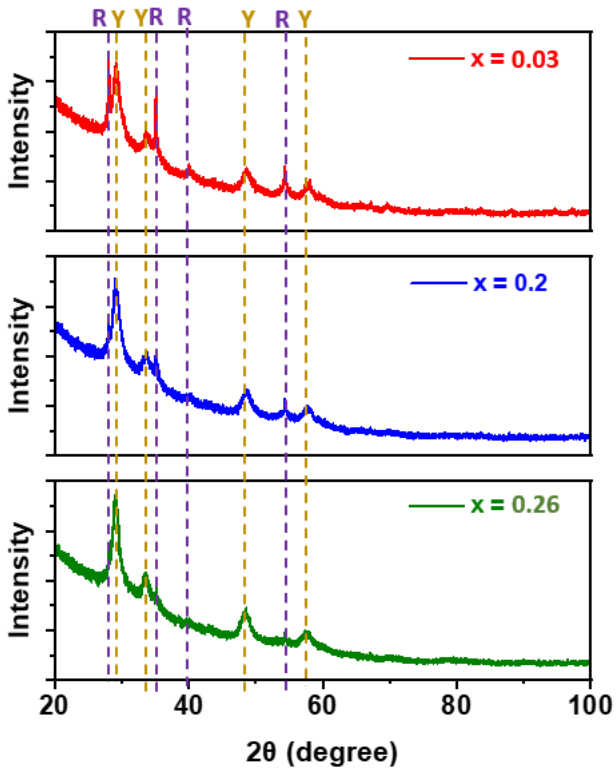

Figure S12. X-ray diffraction patterns after decomposition and subsequent re-oxidation of defect-engineered pyrochlore $Y_2(Y_xRu_{1-x})_2O_{7-\delta}$ electrocatalysts, where x is equal to 0.03, 0.20, and 0.26, respectively. R denotes the diffraction from RuO_2 and Y denotes the diffraction from Y_2O_3.

Table S1. Yttrium and ruthenium precursor amounts for preparing $Y_2(Y_xRu_{1-x})_2O_{7-\delta}$ electrocatalyst series.

Sample (nominal ratio)	**$Y(NO_3)_3{\cdot}6H_2O$ (g)**	**Ru $(NO)(NO_3)_x(OH)_y$ (mL)**
$Y_2Ru_2O_{7-\delta}$	0.383	6.174
$Y_2(Y_{0.1}Ru_{0.9})_2O_{7-\delta}$	0.4213	5.556
$Y_2(Y_{0.2}Ru_{0.8})_2O_{7-\delta}$	0.4596	4.938
$Y_2(Y_{0.3}Ru_{0.7})_2O_{7-\delta}$	0.4979	4.321
$Y_2(Y_{0.4}Ru_{0.6})_2O_{7-\delta}$	0.5362	3.704
$Y_2(Y_{0.5}Ru_{0.5})_2O_{7-\delta}$	0.5745	3.086

Table S2. The atomic ratio between Y and Ru cations based on XRF measurements.

Sample (nominal ratio)	**Y: Ru (measured)**	**Sample (actual ratio)**
$Y_2Ru_2O_{7-\delta}$	49.50: 50.49	$Y_2Ru_2O_{7-\delta}$
$Y_2(Y_{0.1}Ru_{0.9})_2O_{7-\delta}$	51.50: 48.49	$Y_2(Y_{0.03}Ru_{0.97})_2O_{7-\delta}$
$Y_2(Y_{0.2}Ru_{0.8})_2O_{7-\delta}$	59.80: 40.19	$Y_2(Y_{0.2}Ru_{0.8})_2O_{7-\delta}$
$Y_2(Y_{0.3}Ru_{0.7})_2O_{7-\delta}$	62.94: 37.05	$Y_2(Y_{0.26}Ru_{0.74})_2O_{7-\delta}$
$Y_2(Y_{0.4}Ru_{0.6})_2O_{7-\delta}$	66.78: 33.22	$Y_2(Y_{0.34}Ru_{0.66})_2O_{7-\delta}$
$Y_2(Y_{0.5}Ru_{0.5})_2O_{7-\delta}$	70.14: 29.85	$Y_2(Y_{0.42}Ru_{0.58})_2O_{7-\delta}$

Table S3. EIS analysis of $Y_2(Y_xRu_{1-x})_2O_{7-\delta}$ electrocatalysts at 1.58 V in 0.1 M $HClO_4$ aqueous solution.

Electrocatalyst	**R_{sol} (Ω)**	**R_{ct} (Ω)**	**CPE-P,n**	**CPE-T**
$Y_2Ru_2O_{7-\delta}$	31.65	13.79	0.8151	0.001459
$Y_2(Y_{0.03}Ru_{0.97})_2O_{7-\delta}$	30.02	9.265	0.8586	0.000760
$Y_2(Y_{0.2}Ru_{0.8})_2O_{7-\delta}$	26.92	8.278	0.8765	0.000691
$Y_2(Y_{0.26}Ru_{0.74})_2O_{7-\delta}$	30.29	12.49	0.7440	0.000972
$Y_2(Y_{0.34}Ru_{0.66})_2O_{7-\delta}$	29.52	19.05	0.8301	0.000509
$Y_2(Y_{0.42}Ru_{0.58})_2O_{7-\delta}$	29.53	27.8	0.8109	0.000544